Published in final edited form as:
Cell Rep. 2023 September 26; 42(9): 113054. doi:10.1016/j.celrep.2023.113054.

Metabolic transcriptomics dictate responses of cone photoreceptors to retinitis pigmentosa

Sang Joon Lee[1,4,8], **Douglas Emery**[1,8], **Eric Vukmanic**[1,8], **Yekai Wang**[5,8], **Xiaoqin Lu**[1], **Wei Wang**[2], **Enzo Fortuny**[3], **Robert James**[3,7], **Henry J. Kaplan**[6], **Yongqing Liu**[1], **Jianhai Du**[5,*], **Douglas C. Dean**[1,9,*]

[1]Department of Medicine, Brown Cancer Center, University of Louisville Health Sciences Center, Louisville, KY 40202, USA

[2]Department of Ophthalmology and Visual Sciences, University of Louisville Health Sciences Center, Louisville, KY 40202, USA

[3]Department of Neurosurgery, University of Louisville Health Sciences Center, Louisville, KY 40202, USA

[4]Department of Ophthalmology, Kosin University College of Medicine, #262 Gamcheon-ro, Seo-gu, Busan 49267, Korea

[5]Departments of Ophthalmology and Visual Sciences and Biochemistry and Molecular Medicine, West Virginia University, Morgantown, WV 26506, USA

[6]Department of Ophthalmology, St. Louis University School of Medicine, St. Louis MO 63110, USA

[7]Present address: Department of Neurosurgery, University of Indiana School of Medicine, Bloomington, IN 46202, USA

[8]These authors contributed equally

[9]Lead contact

SUMMARY

Most mutations in retinitis pigmentosa (RP) arise in rod photoreceptors, but cone photoreceptors, responsible for high-resolution daylight and color vision, are subsequently affected, causing the most debilitating features of the disease. We used mass spectroscopy to follow ^{13}C metabolites delivered to the outer retina and single-cell RNA sequencing to assess photoreceptor

---

[*]Correspondence: jianhai.du@hsc.wvu.edu (J.D.), douglas.dean@louisville.edu (D.C.D.).

AUTHOR CONTRIBUTIONS
S.J.L., D.E., E.V., J.D., and D.C.D. conceived and designed experiments. W.W. and X.L. performed immunostaining and evaluated glucose transport. S.J.L. followed S cone apoptosis and cone number. E.V. and D.E. performed and analyzed ERGs and collected blood and tissue for ^{13}C analysis. Y.W. performed mass spec, and Y.W., D.E., and J.D, analyzed the results. E.F. and R.J. performed pig catheterization. S.J.L. D.E., E.V., H.J.K., Y.L., J.D., and D.C.D. analyzed results and wrote the manuscript.

SUPPLEMENTAL INFORMATION
Supplemental information can be found online at https://doi.org/10.1016/j.celrep.2023.113054.

DECLARATION OF INTERESTS
The authors declare no competing interests.

transcriptomes. The S cone metabolic transcriptome suggests engagement of the TCA cycle and ongoing response to ROS characteristic of oxidative phosphorylation, which we link to their histone modification transcriptome. Tumor necrosis factor (TNF) and its downstream effector RIP3, which drive ROS generation via mitochondrial dysfunction, are induced and activated as S cones undergo early apoptosis in RP. The long/medium-wavelength (L/M) cone transcriptome shows enhanced glycolytic capacity, which maintains their function as RP progresses. Then, as extracellular glucose eventually diminishes, L/M cones are sustained in long-term dormancy by lactate metabolism.

Graphical abstract

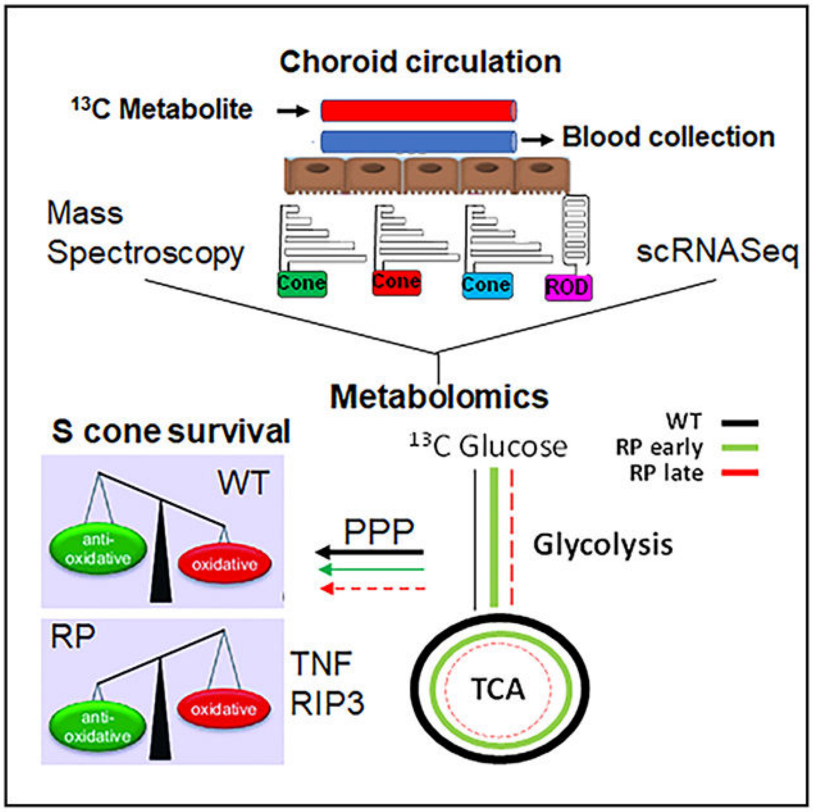

In brief

Lee et al. utilize *in vivo* transport of ^{13}C metabolites to the choroid and single-cell RNA sequencing of photoreceptors to characterize unique photoreceptor metabolomes that drive S cone vulnerability and L/M cone survival during progression of retinitis pigmentosa.

INTRODUCTION

Retinitis pigmentosa (RP) is a hereditary blinding disease affecting as many as 1 in 3,000 individuals.[1] It initiates with loss of rod photoreceptor-dependent peripheral vision and dark adaptation. Accordingly, most RP mutations arise in genes expressed in rods, with the most common targeting the opsin gene *RHO*. Further complicating RP, cone photoreceptors progressively lose their function,[2–5] which is critical for high-resolution daylight and color vision.

As with other neurons, photoreceptors depend on glucose,[6] which is transported from the choroidal circulation via the retinal pigment epithelium (RPE).[5,7] Phosphatidylserine (PS) is externalized on extending outer segment (OS) tips, where it forms complexes with integrins and Tam-family receptor Mertk on the RPE apical surface.[8] Cross-signaling between these receptors leads to activation of Akt, which initiates glucose transport through the RPE to photoreceptors by promoting translocation of the glucose transporter Glut1 to the RPE apical surface.[9] Subretinal injection of OS tip mimetics displaying PS re-activates this Akt/Glut1 pathway in the RPE in RP, restoring glucose transport to the photoreceptors and renewing cone OS synthesis and function in RP after rods are lost. Together, these findings suggest that diminished cone function in RP results from faulty glucose transport because of shortening of abundant rod OS.

We followed cone activity, morphology, and survival in mouse and pig models of RP; in the latter, cones are concentrated in a visual streak functionally resembling the macula.[5,10] As glucose transport to photoreceptors diminishes in RP, we show rapid loss of short-wavelength S cones; however, long/medium-wavelength (L/M) cones survive but gradually lose function. We used mass spectroscopy (spec) to follow ^{13}C metabolites delivered to the outer retina via the choroid circulation, import and export of metabolites to and from the choroid circulation, and single-cell RNA sequencing (scRNA-seq) to compare photoreceptor transcriptomes.

RESULTS

S cones show rapid loss of OS and apoptosis in RP

Rod OS number and length were lost shortly after birth in P23H *RHO* mutant pigs (RP), and rod cell bodies began to diminish by post-natal day 30 (P30).[5,9,11] As with rods, immunostaining for S opsin showed a similar S cone number and OS length in wild-type (WT) and RP pig littermates before birth (Figure 1A), but most S cone OS were lost by P3, and those persisting were significantly shortened (Figure 1B). We then performed TUNEL staining to follow photoreceptor apoptosis. In the pig, the first two outer nuclear layer (ONL) rows of photoreceptors are cones (Figure 1C).[5,9,12] A low level of apoptosis was evident in rods from P1–P14, but there was a burst of apoptosis on P3 in cones (Figures 1D and 1E). Immunostaining for S and L/M opsins showed that S cone cell bodies were diminished by P14, whereas L/M cone numbers did not decrease, demonstrating that apoptosis of S cones was leading selectively to their early loss (Figure 1F). L/M cone OS did not begin to shorten until after P90 (see Figures 6A–6F below), and most L/M cone cell bodies persisted for more than 5 years in RP pigs.[5,9]

Onset of S cone OS loss and apoptosis coincides with diminished glucose transport from the RPE to the outer retina, which initiates in RP with shortening of rod OS by as little as 50%[5,9] (Figure S1). Studies were performed in WT and P23H *Rho* RP mice by following fluorescently labeled 2-deoxyglucose injected into the tail vein. When purified OS or OS mimetics, consisting of liposomes enriched in PS, are injected subretinally in RP, glucose transport from the RPE to photoreceptors is restored (Figure S1), as described previously.[9] Notably, in these experiments, most "glucose" in the retina accumulates in photoreceptor inner segments of the outer retina, with less evident in the inner retina, consistent with photoreceptors as the major sites of retinal glucose metabolism. Taken together, these results are consistent with S cones being more sensitive than L/M cones to diminishing levels of glucose in RP.

An S cone electroretinography (ERG) response diminishes in RP before an L/M cone response

We compared the photopic ERG response in WT and RP pigs. WT and RP pigs were tested with an International Society for Clinical Electrophysiology of Vision (ISCEV) protocol examining cone response to a brief white light flash under photopic conditions (STAR Methods). A similar positive peak arising from L/M cones and initiating at 20 ms was observed in WT and RP out to 3 months of age (Figure 1G), but this L/M cone ERG signal subsequently diminishes in RP.[5,9] An ISCEV protocol has been designed to examine the S cone ERG.[13,14] In this protocol (STAR Methods), L/M cones are first saturated, and then S cone responses to a blue flash stimulus ranging from 0.002–0.06 cd s/m^2 are collected. As reported previously using these conditions,[13,14] we observed a later-arising broad peak at 40–50 ms attributed to S cones (Figure 1G). This peak increased in amplitude with blue flash intensity, and importantly, it was significantly diminished in RP, consistent with decreased S cone number/function (Figure 1G).

scRNA-seq separates human retinal cells into functional clusters

Yan et al.[15] generated 86,253 single-cell transcriptomes from retinas of seven human donors ranging in age from 53–78. We accessed their data deposited in GEO: GSE148077 and from the Single Cell Broad Institute Portal (https://singlecell.broadinstitute.org/single_cell). Based on RNA expression, the cells formed the following clusters in T-distributed stochastic neighbor embeding (tSNE) plots: 3 photoreceptors, 2 horizontal cells, 12 bipolar cells, 25 amacrine cells, 12 retinal ganglion cells (RGCs), as well as non-neural Müller glia, astrocytes, microglia, and endothelial cells[15] (Figure S2). Of these clusters, 49 contained cells from at least six of the seven donors. Expression of the visual pigment genes *RHO, OPN1SW,* and *OPN1LW* highlighted independently clustering rods (6,073 cells), S cones (58 cells), and L/M cones (1,938 cells), respectively (Figures 2A and S2). As a control for scRNA-seq in rods, L/M cones, and S cones, we compared RNA levels of 41 genes identified as a regulatory signature of neurons generally in the photoreceptors (Figure S3). In the mouse, most cones expressing S opsin co-express M opsin, which is quantified in Nadal-Nicolás et al.[16] However, L and M opsin RNA expression was low/not detected in the human S opsin cluster, and when examining all single photoreceptor cells, we failed to identify cells with overlapping S and L/M opsin expression (Figure S3). Thus, as opposed to the mouse, S opsin-only cones appear to predominate in humans.

The L/M cone transcriptome shows enhanced capacity for glucose uptake and glycolysis compared with S cones and rods by expression of RNAs for RdCVF (NXNL1), glycolytic pathways genes, and glycolytic regulators

We compared the metabolic transcriptome aimed at glucose transport and glycolysis in photoreceptor populations. The glucose transporter SLC2A1 (GLUT1) was elevated in L/M cones vs. rods, but it was low in S cones (Figure 2B). However, S cones expressed another glucose transporter, SLC2A3 (GLUT3), which was low in rods and L/M cones. Surprisingly, we found that rod-derived cone viability factor (RdCVF) (NXNL1) RNA, which is thought to be expressed in rods, where the protein is secreted and, in turn, taken up by cones,[2] was expressed in L/M cones but low or not detected in rods, S cones, other retinal neuronal or non-neural cells, or RPE (Figures 2B, S5, and S5A). NXNL1 interacts with glucose transporters to promote glucose entry into cells, allowing cells to maintain glucose uptake as extracellular levels diminish.[2] Notably, L/M cones also expressed elevated levels of RNAs for glycolytic enzymes compared with S cones and rods (Figure 2B). Additionally, HK2, which enhances the initial rate-limiting step in glycolysis, was high in L/M cones, and it was also evident at a lower level in S cones but not in rods. This low level of HK2 in human rods was surprising because it is expressed in rodent rods, where it contributes to essential glycolysis in cells.[3,17] A scatterplot comparing NXNL1 and HK2 RNA expression in photoreceptors illustrates their enrichment in L/M cones (Figure 2B). Likewise, PFKFB3 RNA, whose product is an allosteric enhancer of PFK and, thus, glycolysis, is elevated in S and L/M cones but not detected in rods. Taken together, these results suggest enhanced capacity for glucose import and glycolysis in L/M cones compared with S cones, with rods showing the lowest glycolytic capacity. Comparing rod vs. cone expression in the Human Protein Atlas Proteome provides support for glycolytic capacity differences in this independent dataset (Figure S5B). Nevertheless, a block in glycolysis *in vivo* leads to rapid rod death,[11] demonstrating their dependence upon glycolysis and implying that their seeming low capacity might be a factor in their sensitivity.

Metabolic transcriptomes suggest that rods are restricted to aerobic glycolysis, L/M cones show potential for aerobic glycolysis and oxidative phosphorylation, and S cones rely on oxidative phosphorylation

Consistent with previous findings, RNA for LDHA, which preferentially catalyzes lactate generation from pyruvate, was evident in L/M cones and rods (Figure 2B), suggesting capacity for aerobic glycolysis terminating in lactate production in these photoreceptors. Consistent results were seen when comparing rods and cones in the Human Protein Atlas Proteome (Figure S5B). By contrast, LDHA RNA was low in S cones (Figure 2B), suggesting limited capacity for aerobic glycolysis.

Even though the rod transcriptome suggests a lower capacity for glucose import and glycolysis compared with cones, RNAs for PDHA, which catalyzes the first step of mitochondrial pyruvate metabolism in the tricarboxylic acid cycle (TCA) cycle, and MPC1/2, which transport pyruvate from the cytosol to mitochondria (Figure 3), were low in rods compared with cones, consistent with rod dependence on aerobic glycolysis. By contrast, S and L/M cones expressed RNAs for PDHA as well as MPC1/2, consistent with engagement of the TCA cycle. Despite the transcriptome of rods showing a low level of

MPC1/2 expression and pointing to aerobic glycolysis (Figure 3), mutation of *Mpc1* in mice led to loss of functional rods as well as cones.[18] Notably, this conditional mutation of *Mpc1* was driven by Six3-Cre, and Six3 is expressed early in proliferating retinal progenitors, before they give rise to a common S cone precursor, which, in turn, produces rods and L/M cones.[18,19] Because *Mpc1* mutant retinal progenitors pass through this common S cone precursor on their path to generation of rods and L/M cones, it is conceivable that TCA cycle engagement is critical at this developmental stage for proper functional photoreceptor differentiation from S cone precursors.

Low expression of RNA for LDHA together with high expression of MPC1/2 and PDHA RNAs in S cones suggests that pyruvate from glycolysis is being diverted into the TCA cycle in these cells (Figure 2B). Expression of RNAs for LDHA along with PDHA and MPC1/2 in L/M cones suggests a capacity both aerobic glycolysis and oxidative phosphorylation via the TCA cycle. Consistent with mitochondrial engagement of the TCA cycle and oxidative phosphorylation, expression of nuclear genes for TCA cycle enzymes and those involved in electron transport, as well as ADP/ATP mitochondrial transport and mitochondrial calcium transport, critical for mitochondrial function, are high in cones compared with rods (Figure 3). Additionally, mitochondrial genes (MT) encode key components of electron transport complexes I, III, IV, and V, and these genes are also expressed in S cones and, to a lesser degree, in L/M cones, but expression is low in rods (Figure 3). This low level of expression of genes driving the TCA cycle/electron transport and mitochondrial function suggests that rods rely on glycolysis. Consistent with rod utilization of aerobic glycolysis, more than 90% of glucose taken up by photoreceptors in the rod-rich retina appears to be used for aerobic glycolysis, which drives ongoing OS synthesis.[4,20] Notably, beyond their traditional role in energy production, mitochondria in the ellipsoid of photoreceptors have been shown to act as lenses critical for focusing light on adjacent, visual pigment-rich OS.[21]

The S cone transcriptome shows induction of genes in the fatty acid oxidation pathway and capacity for transcriptionally activating histone methylation that targets these genes

Beyond the capacity for diversion of pyruvate from glycolysis into acetyl-coenzyme A (CoA) in the mitochondrial TCA cycle, the S cone transcriptome selectively shows elevated expression of RNAs for enzymes in the fatty acid oxidation pathway (Figure 3), which also generates acetyl-CoA feeding the TCA cycle. Histone H3K4 trimethylation (me3) is a transcriptional activating mark that is important in driving expression of genes in the fatty acid oxidation pathway.[22,23] Indeed, each of the fatty acid oxidation pathway genes elevated in S cones is a target of H3K4me3 in chromatin immunoprecipitation sequencing datasets (Figure 3)[24] (https://maayanlab.cloud/Harmonizome). KMT enzymes transfer methyl-regulatory groups to histones,[25] and RNAs for family members catalyzing H3K4me3 are selectively expressed in S cones (Figure 4A). Classically, abundant α-ketoglutarate produced by extensive turning of the TCA cycle (e.g., in cones) is an essential co-factor for the KDM family of histone demethylases that erase these histone methylations.[26] However, expression of RNAs for KDM-family enzymes was low/not detected in S cones (Figure 4A), suggesting that the cells lack the capacity to erase histone methylation, thereby shifting equilibrium toward H3K4me3, consistent with activation of fatty acid oxidation. RNAs for KMTs catalyzing histone methylations at H3K9, H3K27, and H3K79 were low/not detected in photoreceptors, as were those for DMNTs and TET enzymes that catalyze DNA methylation/demethylation (Figure 4B).

S-adenosylmethionine (SAM) serves as the methyl donor for KMT-catalyzed histone methylation.[25] It is synthesized from methionine in a reaction catalyzed by MAT2, and consistent with the capacity to generate SAM specifically in S cones, we found that RNA for MAT2B is selectively induced in S cones (Figure 5E). SAM can also be synthesized from phosphatidylethanolamine in a reaction catalyzed by PEMT, but PEMT transcripts were not detected in photoreceptors. Methionine can be synthesized from serine, and it can be regenerated after methyl transfer from SAM in cells via a reaction with betaine, whose source can be dietary. A previous study examining metabolites in the pig circulation showed similar metabolite levels in various arterial sites, whereas altered levels in veins draining an organ compared with the arterial circulation reflected organ-specific metabolism.[27] The ciliary artery feeds the choroid circulation, bringing metabolites and oxygen to photoreceptors in the outer retina, and vortex veins drain quadrants of the choroid.[28] We performed experiments comparing levels of metabolites involved in SAM metabolism in the arterial circulation entering the choroid with levels in the four vortex veins (Figures 5A–5D). We found similar levels of metabolites in arterial blood from the ciliary artery, ear artery, and femoral artery, consistent with previous findings in the pig.[27] Methionine was exported into the choroid circulation, consistent with excess production in the tissue (Figures 5E and S6). RNAs for enzymes catalyzing synthesis of the methionine precursor serine via glycolysis were low in photoreceptors, and accordingly, ^{13}C from glucose was not efficiently incorporated into serine in the outer retina 30 min after injection (Figure 6H). Serine is essential for numerous retinal functions, but retinal serine in the WT mouse appears to be derived primarily from glucose metabolism in the liver. However, under hypoxic conditions in retinopathy of prematurity, serine synthesis in the retina can be induced by Hif1a, which reprograms glycolysis.[29] Accordingly, we observed that serine was imported from the choroid circulation (Figures 5E and S6), with its source possibly synthesis in the liver, as in the mouse. Consistent with ongoing regeneration of methionine following methyl transfer from SAM, betaine was imported from the choroid circulation (Figures 5E and S6). Taken together, these results show that the capacity for SAM synthesis/regeneration from methionine and its utilization in histone methylation is a feature of S cones. We then examined RP pigs on P60, after S cones are diminished, and found that export of methionine was down and that serine and betaine were no longer imported (Figures 5E and S6), consistent with methionine synthesis/regeneration being a property of S cones, as suggested by their transcriptome.

Glucose is imported to the outer retina at the onset of circadian rod OS tip synthesis, and lactate is exported as synthesis is completed

As noted, RPE adjacent to photoreceptors in the outer retina serves as the choroidal circulation outer retinal barrier. In WT pigs, we detected little or no ^{13}C from ^{13}C glucose incorporation into glycolysis or the TCA cycle in the RPE 30 min after injection into the ciliary artery, but incorporation was evident under these condition in the outer retina[9] (Figure 6H). Together, these results suggest that RPE in the WT, under these conditions, is serving primarily to transport glucose from the choroid circulation to photoreceptors.

Additionally, we detected little or no LDHA RNA in the RPE (Figures 2 and S4), also suggesting that they are not a source of lactate generation from pyruvate. RPE expresses high levels of glucose and lactate transporters (Figure 2), allowing it to control extracellular levels of the metabolites in the outer retina via import from and export to the choroid circulation. Notably, however, we found that, in RP, as glucose accumulated in the RPE with transport failure, glycolysis was initiated in the cells, leading into the TCA cycle.[9] Thus, the RPE can switch to glucose metabolism in RP.

To follow metabolite export into and import from the choroid circulation, we again compared arterial metabolite levels entering the choroidal circulation to venous levels in the four vortex veins that drain quadrants of the choroid. In a 12-h on/12-h off light cycle, rod OS tip phagocytosis peaks approximately 2 h after onset of light in the morning, with new OS synthesis commencing soon after.[30] We exposed pigs to such a 12-h light cycle with the “on” cycle initiating at 6:00 a.m., and we evaluated metabolite transport in the morning (8:00 a.m.), at the peak of rod OS tip phagocytosis, and afternoon (3:00 p.m.), designed to approximate completion of new rod OS synthesis. We found that glucose was imported from the choroid circulation in the morning (Figure 5F). As noted, we showed previously that glycolytic metabolites and other metabolites indicative of glucose metabolism are not detected in the RPE, providing evidence showing that un-metabolized glucose is largely being transported from the choroid circulation through the RPE to the outer retina, where it is metabolized.[9] Because glucose transport and subsequent metabolism via aerobic glycolysis are necessary for ongoing OS synthesis,[4,31] we reasoned that its transport from the choroid would diminish as new rod OS synthesis is being completed in the afternoon, and indeed, glucose transport was significantly reduced but still evident in the afternoon (Figure 5F). As a measure of aerobic glucose metabolism in the outer retina during the period of new rod OS synthesis, lactate was transported via the RPE into the choroid circulation in the afternoon, as new rod OS synthesis was being completed (Figure 5F).

L/M cones initially shift toward aerobic glycolysis in RP, and then glycolysis subsides as the cells transition to dormancy

We examined glucose metabolism in the outer retina as RP progressed. Two ages were examined: 3 months, when rods and S cones were lost but L/M cones and their OS were still evident (early RP) and the photopic ERG was still similar to the WT (Figure 1G), and 12 months, when L/M cone cell numbers were still similar, but OS were lost and photopic ERG had diminished in transition to dormancy (late RP) (Figures 6A–6F).[9] We performed experiments injecting ^{13}C glucose into the ciliary artery with the purpose of aiming it via the choroid circulation to the RPE and, in turn, the outer retina (Figures 5A–5C and 6G). After 30 min, ^{13}C incorporation into the outer retina was evaluated. Under these conditions, ^{13}C glucose is rapidly diluted as it exits the choroid, and as evidence it is not incorporated into the retina of the contralateral eye. Such dilution after exiting the eye prevents secondary ^{13}C glucose metabolites from other tissues contributing to retinal metabolism. As anticipated, and reflecting uptake of glucose from the choroid circulation, ^{13}C was incorporated into glycolytic intermediates in the outer retina, but not, as we showed previously, in the RPE under these conditions (Figure 6H).[9] These findings are consistent with photoreceptor metabolic transcriptomes showing capacity for glycolysis in each cell type, but they are a reflection primarily of metabolism in abundant rods in the WT. Beyond glycolysis, ^{13}C was also incorporated into TCA cycle intermediates (Figure 6H). Because the rod transcriptome suggests that the cells are focused on aerobic glycolysis, we concluded that incorporation of ^{13}C from glucose into TCA cycle intermediates reflects cone metabolism, particularly more abundant L/M cones.

With diminished rods and S cones, ^{13}C incorporation into glycolytic intermediates and lactate was still evident in the outer retina in early RP (Figure 6H). Indeed, ^{13}C incorporation into glycolytic intermediates was significantly higher than in the WT (Figure 6H). In this regard, the transcriptome of L/M cones shows enhanced glycolytic capacity compared with rods (Figure 2B), and rods are the predominant photoreceptors in the WT, but L/M comes are the remaining photoreceptor population at 3 months of age in early RP. In contrast to glycolysis, ^{13}C labeling of TCA cycle intermediates was significantly diminished in early RP but still evident, suggesting that L/M cones had transitioned toward aerobic glycolysis terminating in lactate production (Figure 6H). By 12 months of age, we detected little or no ^{13}C incorporation into glycolytic or TCA intermediates in dormant L/M cones (Figure 6H). Taken together, these results suggest that surviving L/M cones first shift toward aerobic glycolysis in RP, and then glycolysis ultimately diminishes as the cells transition to a dormant state, reflected by loss of OS and ERG (Figure 6I).

TCA intermediates can be exported out of mitochondria via SLC25A transporters, where they have key roles in biologic processes such as fatty acid and lipid synthesis as well as regulation of histone modifications in gene expression.[32] As these intermediates build up in the cytoplasm, they can be exported from cells, and an example of such export from the outer retina is succinate, which can be oxidized and taken up and utilized by the RPE to uncouple electron transport from ATP synthesis.[33,34] We noted induction of SLC25A RNA in cones vs. rods (Figure 6J), and as a measure of TCA cycling, we compared export of TCA intermediates from the outer retina to the choroid circulation in WT and early RP. Consistent with diminished turning of the TCA cycle in early RP, we found a decrease in TCA intermediates exported to the choroid circulation (Figure 6K).

Cone transcriptomes show capacity for lactate import and metabolism

Despite reduced LDHA RNA, S cones express LDHB RNA (Figure 2), which preferentially has higher affinity for lactate vs. pyruvate than LDHA and is required to catalyze the reverse reaction, generating pyruvate from lactate in cancer.[35] Expression of LDHB RNA in S cones suggests their potential to utilize extracellular lactate in addition to glycolysis and fatty acids to further fuel the TCA cycle. Consistent with their potential to import extracellular lactate, S cones express RNAs for bidirectional lactate transporters (Figure 2). Like S cones, L/M cones also express RNAs for LDHB and lactate transporters (Figure 2), and their expression of PDHA and TCA/electron transport transcripts suggests that L/M cones can divert pyruvate not only from glycolysis but also potentially from lactate metabolism into oxidative phosphorylation.

Lactate is imported from the choroid circulation during the period of new cone OS synthesis

The cone OS tip phagocytosis/new OS synthesis cycle is thought to be approximately 12 h out of phase with that in rods in this diurnal process, with phagocytosis peaking in the early evening, approximately 4 h after the afternoon time point at 3:00 p.m., and new OS synthesis initiating thereafter.[36] Thus, as rod OS tip phagocytosis is peaking in the morning, new cone OS synthesis is ongoing. Notably, as opposed to the afternoon, we found that lactate was imported from the choroid circulation in the morning (Figure 5F). This finding confirms the RPE as a circadian bidirectional transporter of lactate *in vivo*, and this lactate uptake during the period of cone OS synthesis is consistent with cone transcriptomes that point toward usage of lactate as a fuel source. Because of the phasic difference in rod and cone OS tip phagocytosis/new OS synthesis, extracellular lactate generated from aerobic glycolysis during the period of new rod OS synthesis, which we show is exported into the choroid circulation at 3:00 p.m., would seemingly not be available to cones as they initiate synthesis of new OS after their peak of phagocytosis in the evening.

^{13}C from circulating lactate is not detected in metabolites in the RPE, but it is incorporated into TCA cycle intermediates in the outer retina at similar levels in the WT and RP

We performed similar experiments injecting ^{13}C lactate and found little or no ^{13}C incorporation in TCA cycle intermediates in the RPE in either the WT or RP (Figure 6L), suggesting that the cells are primarily transporting lactate between the choroid circulation and outer retina under these experimental conditions. By contrast, ^{13}C from lactate was incorporated into TCA cycle intermediates in the outer retina (Figure 6M), consistent with its metabolism by photoreceptors. Because we found low LDHB transcripts in rods (Figure 2B), we concluded that cones are likely responsible for this lactate metabolism. Indeed, ^{13}C incorporation from lactate into the outer retina was not significantly different in RP after rods were lost (Figure 6M), suggesting that, unlike glucose, its transport from the choroid circulation via the RPE is not compromised in RP. We concluded that, with glycolysis diminished in RP, L/M cones continue to utilize lactate imported from the choroid circulation as fuel.

Diminished TCA cycle in RP impedes cone glutamate synthesis

Glutamate is the neurotransmitter released by all photoreceptors.[37] Its level in photoreceptors can be maintained by reabsorption of secreted/extracellular glutamate[38] or by *de novo* synthesis from glutamine or TCA cycle intermediates.[39] Rods show diminished capacity for the TCA cycle compared with cones, and they express little or no RNAs for GOT1/2 in generating glutamate from TCA cycle oxaloacetate via aspartic acid or RNAs for GLUD1/2 for its synthesis from α-ketoglutarate (Figure 2B). Further, rods showed little or no expression of RNAs for GLS or SLC38-family GLN transporters (Figure 2B), suggesting limited capacity to synthesize glutamate from glutamine. Accordingly, injection of ^{13}C glutamine into the choroid circulation, as shown in Figure 6G, led to little detectable ^{13}C incorporation into glutamate in the WT outer retina, where rods predominate (Figure 6N). Evaluating glutamate uptake from and export into the choroid circulation in the morning and afternoon, as shown in Figure 5F, showed that it was exported into the circulation in the afternoon, consistent with an excess of glutamate in the outer retina (Figure S6). By contrast, glutamate was imported from the choroid circulation in the morning (Figure S6), as rods take up glutamate with the onset of light. This uptake of glutamate in the morning was dependent on rods and was lost in RP (Figure S6). Together, these results are consistent with rods utilizing imported glutamate from the choroid circulation in response to light onset in the morning.

By contrast, cones express RNAs for GOT1/2 (Figure 3) and thus have the capacity to synthesize glutamate from aspartic acid arising from the TCA cycle via the malate-aspartate shuttle, which moves aspartate and glutamate between the mitochondria and cytoplasm. However, S cones and most L/M cones express little RNA for GLUD1/2, which catalyze synthesis of glutamate from α-ketoglutarate. Consistently, we found that ^{13}C from glucose was efficiently incorporated into aspartic acid and glutamate in the WT outer retina (Figure 6H). Because rods have reduced expression of RNAs for enzymes catalyzing this synthesis, we concluded that this ^{13}C incorporation is likely occurring in cones. We then injected ^{13}C glutamine in early RP, where L/M cones are the remaining photoreceptors. Despite expression of GLS and glutamine transporters in cones from the WT (Figure 3), we failed to detect ^{13}C from injected ^{13}C glutamine in glutamate in early RP (Figure 6N), suggesting that glutamate synthesis from glucose via aspartic acid in the malate-aspartate shuttle is an important source of glutamate in cones. Notably, the malate-aspartate shuttle acts to transfer reducing equivalents from NADH in the cytosol to the mitochondria because the mitochondrial membrane is impermeable to NADH and NAD^+. This transfer of reducing equivalents is essential for maintaining the favorable NAD^+/NADH ratio required for mitochondrial oxidative metabolism of glucose.[40] Further, the malate-aspartate shuttle is essential for glutamate synthesis in CNS neurons, where it is necessary to maintain functional neurotransmitter levels at the synaptogenic membrane.[41] Notably, ^{13}C from glucose incorporation into aspartic acid and glutamate diminished in early RP, coincident with a decrease in TCA intermediates, and in late RP, persisting L/M cones had lost the capacity to synthesize glutamate from glucose (Figure 6H). We then concluded, with reduced TCA cycling in cones in early RP, that the malate-aspartate shuttle diminishes, limiting their ability to synthesize glutamate from glucose, which is further diminished in late RP.

The S cone transcriptome shows induction of pentose phosphate pathway (PPP) and oxidative stress response genes linked to a MAT2A-H3K36 methylation loop

As discussed above, the S cone transcriptome suggests that glycolysis, fatty acid oxidation, and lactate feed into the TCA cycle in these cells (Figures 2B and 3). Beyond ROS generation from extensive utilization of the electron transport chain, the mitochondrial fatty acid oxidation pathway also generates ROS.[42] The PPP is a first-line defense against reactive oxygen species (ROS).[43] The oxidative arm of the PPP catalyzes reactions that lead to increased NADPH for the antioxidant capacity to reduce ROS species, and RNAs for PPP enzymes are elevated in S and L/M cones (Figure 7A). Additionally, products catalyzed by TALDO1 in the non-oxidative arm can feed into the oxidative arm for NADPH generation. In a similar fashion, RNAs for genes sensing and mounting the cellular response to ROS are induced (Figure 7A). Together, these findings point to an ongoing response to ROS that is most evident in S cones and also seen in L/M cones but not rods.

Like H3K4me3, H3K36me3 is an epigenetic mark that promotes gene transcription.[44] Notably, H3K36me3 is important in transcription of genes responding to ROS.[45,46] As with H3K4, RNAs for KMT writers of H3K36 methylation are selectively induced in S cones, and KDM-family erasers of this methylation are low/not detected (Figure 4A), suggesting a balance tipped toward H3K36me3 in the cells. Consistently, several key genes in the PPP, as well as most ROS sensors/responders induced in S cones, are targets of H3K36me3 (Figures 2B and 7A)[24] (https://maayanlab.cloud/Harmonizome). Similarly, the gene for MAT2A, which catalyzes synthesis of the histone methyl donor SAM and whose RNA we show is expressed selectively in S cones, is also a target of H3K36me3 (Figure 7B), suggesting a positive MAT2A-H3K36me3 loop. Because SAM is a general histone methylation donor, such a MAT2A-H3K36me3 loop might be consequential for KMT-catalyzed methylation of other histone amino acids, including H3K4.

As noted above, methionine can be regenerated from S-adenosyl-homocysteine (SAH) after SAM methyl transfer to histones (Figure 5E). However, accumulating SAH from ongoing methyl transfer can also generate cystathionine, cysteine, and, ultimately, GSH and taurine for ROS protection (Figure 7B), linking ongoing SAM methyl transfer to ROS protection. Consistent with generation of cystathionine, cysteine and taurine, we found each of these metabolites is exported to the choroid circulation (Figures 7B and S9). We then examined levels of GSH and oxidized GSH (GSSG) arising from ROS neutralization using mass spec. Glutathione synthetase (GSS) RNA is enriched in S cones, and, like MAT2A, it is a target of H3K36me3. The ratio of GSSG to GSH in the retina increased from 2:1 in the WT to 5:1 in RP (where rods and S cones are lost), coincident with diminished levels of the PPP marker ribulose-5 phosphate (RPIA) (Figure 7C). As noted above, NADPH generated from the PPP is utilized for reduction of GSSG to regenerate GSH. Together, these results suggest that ROS oxidation of GSH to GSSG increases in the retina as the PPP diminishes in RP. Because accumulating ROS leads to inhibition of TCA cycle enzymes,[47] such an increase in ROS, as evidenced by the diminished GSH:GSSG ratio and diminished PPP marker, likely accounts for the decrease in TCA cycle intermediates in L/M cones as RP progresses (Figure 6H). Notably, GSSG in RPE increased in RP, as did RPIA (Figure 7C), consistent with onset of a PPP response to initiation of ROS production in these cells in RP.

S cones show increased capacity for alternative RNA splicing

Beyond initiating a gene expression response to ROS, H3K36me3 classically drives expression of genes regulating alternative RNA splicing.[44,48] Notably, neurons display one of the highest levels of alternative splicing, and this is particularly evident in splicing of micro-exons (≤27 nt), which frequently include sites of protein activity-regulating modifications such as phosphorylation.[49–51] We examined expression of RNAs known to be alternatively spliced in neurons, including several involved in ciliogenesis, and found that they are generally enriched in S cones (Figure S7). However, none of these genes are targets of H3K36me3 (Figure S7) (https://maayanlab.cloud/Harmonizome),[24] indicating that their preferential expression in S cones is not driven by H3K36me3. As with RNAs targeted for alternative splicing, we found that splicing regulatory factors that drive this alternative splicing are selectively induced in S cones, but in contrast to RNAs targeted for alternative splicing, most of these splicing regulator factor genes are targets of H3K36me3 (Figure S7). Interestingly, a previous study in mice of splicing and splicing factor expression during photoreceptor development found that the MSI family (MSI1/2) appears to specifically regulate alternative splicing as photoreceptor progenitors become post-mitotic in their transition to S cone precursors, which, in turn, give rise to rods and L/M cones.[52,53] We found, in adult human photoreceptors, that MSI2 RNA is selectively expressed in S cones along with other splicing factors, including the micro-exon splicing regulators SRRM3/4 (Figure S8), critical for alternative splicing and cilium generation in cones.[54] Taken together, these finding suggest that the enhanced splicing capacity evident in S cone precursors is retained in mature S cones but diminished with rod and L/M cone differentiation.

A picture of how such an H3K36me3-driven alternative splicing program might be linked to photoreceptor differentiation and particularly S cone function is still lacking, but such alternative splicing programs are central to CNS development and IPS cell reprograming.[55,56]

Tumor necrosis factor (TNF) and activated RIP3 highlight apoptotic S cones in RP

TNF can initiate apoptosis, and it has been shown to be the first protein induced in dying photoreceptors following light damage and retinal detachment.[57–59] Notably, TNF is induced in response to glucose starvation, and it is responsible for subsequent cell death.[60] Although TNF was not detected in the WT or RP retina before birth, it was induced specifically in S cones undergoing apoptosis shortly after birth in RP, and it diminished as S cones were lost (Figures 7D–7F). TNF causes a reversal of electron transport through complex I, leading to ROS production.[61] RIP3 is activated by phosphorylation of S227 downstream of TNF to mediate this ROS production by targeting the activity of enzymes in the TCA cycle. Accordingly, S227 phospho-RIP3 was induced along with TNF in S cones (Figures 7G–G″). Further, TNF and RIP3 RNAs were also induced in the RP retina in a similar time course (Figures 7H and 7I). In a feedback loop, TNF-RIP3 also induces KDM enzymes to erase H3K36me3, leading to loss of the protective PPP response to ROS.[62] We concluded that TNF-RIP3 expression in S cones in response to diminishing glucose in RP is likely responsible for mitochondrial dysfunction leading to a burst of ROS production while diminishing the capacity of the cells to respond to ROS via the PPP (Figure 7J). Given their ongoing battle against ROS, TNF-RIP3 induction in S cones likely tips their balance toward early death (Figure 7J). Although we did not observe TNF-RIP3 expression in rods in this early stage of RP, it is easy to see how it might impact the cells later as ER stress begins to accumulate in response to *RHO* mutation. However, our findings suggest that rods do not appear to engage the TCA cycle; thus, any negative effects of TNF in rods would appear to be independent of the reversal of electron transport through complex I to generate ROS.

DISCUSSION

Glucose transport from the choroid via the RPE to photoreceptors in the outer retina becomes more restricted as RP progresses. Glucose is important in cones not only for new OS synthesis but, as we show here, for synthesis of the key neurotransmitter glutamate and mounting a response to ROS via the PPP. S and L/M cones respond differently to diminishing glucose levels as RP progresses. S cones rapidly lose OS and undergo apoptosis. Although L/M cones eventually lose their OS and function, they survive in a dormant state, where function can be restored by reestablishing extracellular glucose.

The S cone metabolic transcriptome suggests that three pathways converge on the TCA cycle: glycolysis, lactate metabolism, and fatty acid oxidation. The resulting high level of oxidative phosphorylation via extensive usage of the electron transport chain would be expected to generate ROS, and beyond driving ROS production via electron transport, lactate can also interact with iron non-enzymatically to generate ROS.[63] Left unchecked, ROS triggers apoptosis. Consistent with a response to ongoing ROS generation in S cones, the cells show induction of key PPP genes as well as sensors of and responders to ROS.

H3K36me3 is important for induction of ROS sensors/responder genes, and we show that key PPP genes as well as ROS sensor/responder genes induced in S cones are H3K36me3 targets. KMT enzymes utilize methyl groups from SAM to catalyze histone methylation, and we show that induction of MAT2, which catalyzes SAM synthesis from methionine, and enzymes that catalyze H3K36me3 are specifically expressed in S cones. In a positive loop, genes catalyzing SAM and GSH synthesis are targets of H3K36me3. Together, this metabolome allows S cones to manage ROS produced from extensive oxidative phosphorylation. However, with glucose deprivation and the resulting TNF-RIP3, which reverses electron transport through complex I to generate a burst of ROS and induces KDMs to demethylate H3K36, the balance rapidly shifts toward S cone apoptosis early in RP.

The L/M cone metabolic transcriptome shows enhanced capacity for glucose transport and glycolysis, which, we contend, allows it to continue glycolysis and function for some time as extracellular glucose diminishes in RP. Even though L/M cones eventually transition to a dormant state lacking glycolysis and OS, our results suggest that they continue to metabolize lactate, which, we suggest, allows their long-term survival and, thus, potential for restoration of function when extracellular glucose is re-established. Although the rod transcriptome suggests lack of capacity to metabolize lactate, loss of lactate transporters on rods or RPE nevertheless inhibits rod function.[64] Taken together, these results suggest that export of lactate generated by aerobic glycolysis from rods and its transport via the RPE to the choroid circulation is important to maintain rod function.

Although S cones are a minor population of photoreceptors in the adult, as noted above, during photoreceptor development, a population of S cone precursors forms, which, in turn, gives rise to rods and L/M cones.[19,65] Thus, the S cone transcriptome might reflect a precursor baseline whose changes in rods and L/M cones reflect pathways mediating their differentiation. Indeed, H3K4 methylation, reflected by the S cone transcriptome, must be diminished for transition of S cone precursors to rods,[66] whose transcriptome, we show, lacks H3K4 methylation capacity.

Limitations of the study

Our results focus on photoreceptor and RPE transcriptomes and mechanisms leading to sequential loss of S and M cone function in P23H *RHO* RP. It will be important to extend these findings to other RP mutations and other retinal diseases. Multiple studies point to regulation of glucose metabolism as a key feature in RP progression. Our studies here suggest importance of lactate as a fuel for cones in end-stage RP as glycolysis diminishes, indicating that pathways linking these metabolites might be important therapeutic targets.

STAR★METHODS

RESOURCE AVAILABILITY

Lead contact and materials availability—Further information and requests for resources and reagents should be directed to and will be fulfilled by the lead contact, Douglas C. Dean (douglas.dean@louisville.edu).

Materials availability—This study did not generate new unique reagents.

Data and code availability

- All data reported in this paper will be shared by the lead contact upon request.
- This paper does not report original code.
- Any additional information required to reanalyze the data reported in this paper is available from the lead contact upon request.

EXPERIMENTAL MODEL AND SUBJECT DETAILS

Experimental design—We used mass spec to follow metabolism of ^{13}C metabolites delivered to the outer retina via the choroid circulation and import and export of metabolites from and into the choroid circulation in WT and RP pigs. Immunostaining for cone opsins and TUNEL staining were used to follow cone number and morphology during RP progression. Cone electrophysiology was followed by ERG. Number and ages of animals are shown in legends.

Randomization—Littermates were divided into WT and RP groups for experiments. We did not detect differences in female vs. male RP mice or pigs in measurements described above, thus males and females were randomly included into study groups.

Humans—86,253 cells were collected from retinas of seven human donors ranging in age from 53 to 78. All donors were confirmed to have no history or clinical evidence of ocular disease or intraocular surgery. Briefly, eyes were collected 3–14 h postmortem through the Rapid Autopsy Program, Massachusetts General Hospital. The anterior segment was removed followed by further dissection and cell dissociation. Single cell suspensions were diluted to 500–1800 cells/μL in 0.04% BSA/Ame for loading into 10X Chromium Single Cell v2 or v3 Chips. Following collection, cDNA libraries were prepared and sequenced on an Illumina HiSeq 2500. Acquisition and use of postmortem human tissue samples was approved by the Human Study Subject Committees of Harvard Medical School

(DFCI Protocol Number: 13–416 and MEE – NHSR Protocol Number 18–034 H) and in compliance with the National Human Genome Research Institute (NHGRI) policies. Informed consent was obtained from participants if they were enrolled antemortem or their legal guardians if postmortem.

Mice—All methods regarding mice were approved by the University of Louisville Institutional Animal Care and Use Committee and adhered to the ARVO Statement for Use of Animals in Ophthalmic and Vision Research. WT and P23H *Rho* mutant mice[67] https://www.jax.org/strain/017628 littermates were compared in the studies. Ages are stated in figure legends. In previous studies we did not detect any difference in assays utilized here based on gender. So, male and female mice were assigned to control and experimental groups without regard to gender.

Pigs—All methods regarding pigs were approved by the University of Louisville Institutional Animal Care and Use Committee and adhered to the ARVO Statement for Use of Animals in Ophthalmic and Vision Research. WT and P23H *RHO* mutant pigs[5,10] littermates were compared in the studies. Ages are stated in figure legends. In previous studies we did not detect any difference in assays utilized here based on gender. So, male and female pigs were assigned to control and experimental groups without regard to gender.

METHOD DETAILS

Retina histology and RNA analysis—Pigs were euthanized by ear vein injection of beuthanasia (a mixture of sodium pentobarbital sodium and sodium phenytoin, 0.1mL/lb) through an ear vein catheter after sedation with Ketamine/Dexmedetomidine/Atropine. Embryos were delivered by caesarian section from the euthanized pregnant sows. Both eyes from at least three pigs were used for each time point. Eyes were enucleated and immediately immersed in the CO2-independent media on ice. The anterior segment was removed and the eye cup for cryosection was fixed in 4% (w/v) paraformaldehyde in 0.1 M phosphate buffer for 20 min followed by three washes with 0.1 M phosphate buffer. Tissues were then cryoprotected through 30% sucrose for overnight. Each retina was bisected along the horizontal plane through the dorsal margin of the optic disc and vertically cut through the optic disc. Each of the four pieces was notched on its dorsal edge to preserve orientation. For frozen sections, retinas were embedded with polyvinyl alcohol, polyethylene glycol-based Optimal Cutting Temperature cutting reagent (OCT):20% sucrose (2:1). Serial sectioning was performed at 12 μm on a cryostat and tissues were mounted on Super-Frost glass slides. Retinas for paraffin sections were fixed with 10% formalin for 48 h. The retinas were then imbedded with 3% agar gel in 5% formalin and reoriented transversely, then dehydrated in 70% ethanol for paraffin embedding. The tissues were cut at 5μm and H&E staining were performed every fifth slide. For immunostaining, frozen sections of swine retina were dried at 37°C for 20 min followed by a rinse through phosphate buffered saline (PBS) for 5 min. The samples were then blocked with 2% bovine serum albumin (BSA), 5% serum and 0.1% Triton X-100 at 25°C for 1 h, then incubated with primary antibody at 4°C overnight. After primary antibodies had been removed and the samples washed, secondary antibodies were applied for 1 h at 25°C. Images of stained retina sections were captured with a Zeiss confocal microscope, and the images adjusted for contrast and brightness with

Adobe Photoshop v9.0.2. As a negative control, no immunostaining was evident in the absence of primary antibodies. Primary antibodies: Rabbit TNFa abcam 183218; Rabbit RIP3 S227 activation 209384 abcam; rabbit anti-L/M opsins (Millipore, 1:400) Cat#: AB 5405; rabbit anti-S opsin (Millipore, 1:400) Cat#: AB5407; rabbit anti-NRL (gift from Anand Swaroop, National Eye Institute, Bethesda, MD, 1:1000); chicken anti-JH492 and JH 455 (gifts from Jeremy Nathans, Johns Hopkins Medicine, Baltimore, MD, 1:5000). Bound antibodies were visualized with either Alexa fluor 488- (Invitrogen, 1:500) or Alexa Fluor 568- (Invitrogen, 1:500) conjugated secondary antibodies. Nuclei were counterstained with 4’,6-diamidino-2-phenylindole (DAPI). The number of cones (S and L/M) and TUNEL+ cells was counted following immunostaining in six different locations through the visual streak in sections cut through the optic nerve superior to inferior. n = 3. For TUNEL staining, we used a commercially available fluorescent TUNEL kit (DeadEnd Fluorometric TUNEL System, G3250; Promega, USA) according to the manufacturer’s instructions. The cell nuclei were counterstained with DAPI.

RNA was extracted using TRIzol (Invitrogen, Carlsbad, CA). cDNA was synthesized using the Invitrogen RT Kit according to the manufacturer’s protocol (Invitrogen). Real-time quantitative PCR was performed using the Mx3000P Real-Time PCR System (Stratagene, Cedar Creek, TX) according to the manufacturer’s instructions.

Blood collection—Where indicated, WT and RP pigs were maintained on a 12 h on/12 h off light cycle initiating at 6:00 a.m. for 14 days prior to experiments. Groups were fasted for 18 h before blood or tissue collection. Anesthesia was initiated with a combination of telazol, ketamine, and xylazine (1.25–2.5 mg/kg of each agent in a single injection) followed by intubation and maintenance of surgical plane of anesthesia with inhaled isoflurane (1.0%–5.0%). Sterile hypromellose ophthalmic demulcent solution was applied to both eyes and the eyes taped shut to maintain lubrication while under anesthesia. Arterial blood collection is described under “femoral artery catheterization.” To collect blood from the vortex veins, a lateral canthotomy was performed for greater exposure of the posterior of the eye. The conjunctiva was removed with hemostasis achieved by applying pressure to the areas of bleeding with a sterile cotton-tipped swab. The superior and inferior rectus muscles were then isolated and tied off with sutures for manipulation of the eye to access each of the four vortex veins. A vortex vein is located and punctured by a sterile needle with blood collected into a heparinized capillary tube to eliminate clotting. Pressure to the vortex vein was applied using sterile cotton-tipped swab to achieve hemostasis. The eye is also kept constantly moist with the application of balanced saline solution between subsequent collection sites. Typically, the vortex veins were collected in order by superonasal, inferonasal, inferotemporal, and superotemporal. The animal was turned to the other side for access to the contralateral eye and the blood collection process repeated. After the completion of the blood sampling, the eyes were enucleated for further processing and the animal euthanized. Blood samples were centrifuged for 10 min at 1,000–2,000 × g with the resulting plasma transferred to a sterile collection tube.

ERG measurements—WT and RP pigs were held in a steady plane of isoflurane-induced anesthesia (Wang et al., 2019; Wang et al., 2016; Ross et al., 2012), and an electrophysiology system equipped with a Veris Ganzfeld V2 Stimulator driven by Veris software (Electrodiagnostic, Inc.) was used. ERG-JET corneal electrodes (fabrinal; supplied by LKC Technologies) were placed on the corneal surface to capture full-field ERG responses of light-adapted swine under photopic conditions. Swine were light-adapted to the standard ISCEV background of 30 cd/m^2 for 10 min prior to data acquisition. This adaptation period is designed to minimize contributions of rods to the photopic flash ERG. After the initial 10-min adaptation period, photopic cone-mediated ERG waveforms arising primarily from L/M cones were recorded in response to ISCEV standard flashes of 3 cd s/m^2. Pigs were then analyzed using an ISCEV-based protocol for isolation of an S cone response.[13] Under photopic conditions, pigs were acclimated to an LED stimulus ranging at 570 or 627nm (with similar results) at 233 cd/m^2 stimulus for 5 min prior to presentation of blue flash stimuli (LED: 455nm) ranging from 0.002–0.06 cd s/m^2. ERG responses were collected in stepwise manner beginning with the lowest flash intensity.

Femoral artery catheterization—Animals were fasted for 12 h. Then, ciliary artery catheterization was performed with pigs under general anesthesia, positioned on a radiolucent table in the fluoroscopy suite, as described in detail previously.[68] Briefly, femoral artery access in the inguinal area was obtained using the modified Seldinger technique and a 5 French Stiff Micropuncture Access Set (Cook Medical; G48008 or G35551), which was exchanged for a standard 5 Fr 10 cm length femoral sheath. A 5-Fr diagnostic angiography catheter (with a Vert, Berenstein, Simmons-2, or Cobra) was advanced over a 0.35″ guidewire in retrograde fashion along the abdominal and then thoracic aorta, over the aortic arch, prior to engaging the origin of the brachiocephalic/common carotid artery. The catheter was then advanced over the guide wire into the internal carotid artery and positioned just proximal to the petrous portion of the artery. The guide wire was removed and digital subtraction angiography was used to identify the ophthalmic artery on the ipsilateral side. A standard 0.014″ microwire was placed within a 0.17″ inner diameter microcatheter and the combined microcatheter/microwire system advanced under live fluoroscopy with the microwire leading and accessing the ophthalmic artery. The microwire was then pinned in position and the microcatheter was advanced over the microwire to selectively catheterize the ophthalmic artery of interest. The microwire was removed, digital subtraction angiography used to confirm that the microcatheter tip was within the ophthalmic artery, in place for serum collection and infusion of ^{13}C metabolites. At the conclusion of the procedure, all catheters, wires and the femoral sheath were removed and hemostasis was achieved by manual compression of the femoral puncture. Standard radiation safety procedures with optimized shielding were followed to protect researchers and staff from direct and scatter radiation.

40% 13C glucose or 20% lactate or glutamine in 2 mL was delivered in 30 min via ciliary artery-placed microcatheter and 13C incorporation into metabolites in the retina and RPE of WT and RP was analyzed 30 min later. Notably, 13C incorporation into metabolites in the contralateral eye was not detected, demonstrating that 13C metabolites are diluted as they leave the eye and thus metabolites from other tissues are not contributing to retinal metabolism under these conditions. At 1 h following injection, we began to detect metabolites indicative of multiple turns of the TCA cycle, thus we chose the 3o min time point for retinal and RPE collection and analysis.

LC/MS/MS—Mouse and pig retinas and RPE from WT and RP animals were extracted for metabolites.[18,69,70] Extracts were loaded into Biocrates MxP Quant 500 96 well plates designed for analysis of up to 630 metabolites, as described in the user manual (Biocrates.com). These plates included zero, blank and loading controls as well as metabolite concentration calibration standards, and results were analyzed using MetIDQ software. MetIDQ includes a target normalization procedure based on quality controls for batch-to-batch and plate-to-plate correction. Analysis was done using Shimadzu LC Nexera X2 UHPLC coupled with a QTRAP 5500 LC MS/MS (AB Sciex). The mobile phase was (A) water with 0.2% formic acid and (B) acetonitrile 0.2% formic acid (All solvents were LC–MS Optima grade from Fisher Scientific, formic acid was purchased from Honeywell Fluka). A MxP Quant 500 kit column system was used for chromatographic separation. Samples were run into this column system in positive (LC1) and negative (LC2) polarity. The gradient elution for LC1 is 0.8 mL/min of 0% B, going from 0 to 12% B at 0.25 to 1.5 min, 12%–17.5% B at 2.7 min, 17.5–50% B at 4 min, 50–100% at 4.5min, flow rate increasing to 1 mL/min at 4.7min and 5 min, 100-0% B at 5.1 min, and flow rate decreasing to 0.8 mL/min at 5.8min. The source and collision gas was N2. The ion source conditions in LC1 were: curtain gas (CUR) = 45 psi, collision gas (CAD) = high, ion spray voltage (IS) = 5500 V, temperature (TEM) = 500°C, ion source gas 1 (GS1) = 60 psi, and ion source gas 2 (GS2) = 70 psi. The gradient elution for LC2 is 0.8 mL/min of 0% B, going from 0 to 25% B at 0.25 to 0.5 min, 25%–50% B at 2 min, 50–75% B at 3 min, 75–100% at 3.5min, flow rate increasing to 1 mL/min at 4.7min and 5 min, 100-0% B at 5.1 min, and flow rate decreasing to 0.8 mL/min at 5.8min. The source and collision gas was N2. The ion source conditions in LC1 were: curtain gas (CUR) = 20 psi, collision gas (CAD) = high, ion spray voltage (IS) = −4500 V, temperature (TEM) = 650°C, ion source gas 1 (GS1) = 40 psi, and ion source gas 2 (GS2) = 40 psi. No column was used for FIA injections. The gradient elution for FIA1 (positive) and FIA2 is 0.03 mL/min of 100% B, holding this condition to 1.6 min, then increasing flow rate to 0.2 mL/min at 2.4min, holding this condition until 2.8 min, then decreasing the flow to 0.03 min at 3min. The source and collision gas was N2. The ion source conditions in FIA1 and FIA2 mode were: curtain gas (CUR) = 30 psi, collision gas (CAD) = high, ion spray voltage (IS) = 5500 V, temperature (TEM) = 200/350°C, ion source gas 1 (GS1) = 40/30 psi, and ion source gas 2 (GS2) = 50/80 psi (FIA1/FIA2).

For LC/MS/MS runs that did not utilize Biocrates plates, an ACQUITY UPLC UPLC BEH Amide analytic column (2.1 × 50 mm, 1.7 μm, Waters) was used for chromatographic separation. The mobile phase was (A) water with 10 mM ammonium acetate (pH 8.9) and (B) acetonitrile/water (95/5) with 10 mM ammonium acetate (pH 8.2) (All solvents were LC–MS Optima grade from Fisher Scientific). The total run time was 11 min with a flow rate of 0.5 mL/min with an injection volume of 5 μL. The gradient elution is 95–61% B in 6 min, 61–44% B at 8 min, 61–27% B at 8.2 min, and 27–95% B at 9 min. The column was equilibrated with 95% B at the end of each run. The source and collision gas was N2. The ion source conditions in positive and negative mode were: curtain gas (CUR) = 25 psi, collision gas (CAD) = high, ion spray voltage (IS) = 3800/- 3800 V, temperature

(TEM) = 500°C, ion source gas 1 (GS1) = 50 psi, and ion source gas 2 (GS2) = 40 psi. Each metabolite was tuned with standards for optimal transitions, and ^{13}C-nicotinamide D4 (Toronto Research Chemicals) was used as the internal standard and extracted MRM peaks were integrated using MultiQuant 3.0.2 software (AB Sciex) and corrected for ^{13}C-nicotinic acid.

GC/MS—Metabolites were derivatized by methoxyamine hydrochloride followed by N-tertbutyldimethylsilyl-N-methyltrifluoroacetamide (TBDMS) as described.[18,69,70] An Agilent 7890B/5977 B GC/MS system with an Agilent DB-5MS column (30 m × 0.25 mm × 0.25 μm film) was used for GC separation and analysis of metabolites (5). Ultra–high-purity helium was the carrier gas at a constant flow rate of 1 mL/min. The temperature gradient started at 95°C with a hold time of 2 min and then increased at a rate of 10°C/min to 300°C, where it was held for 6 min. The temperatures were set as follows: inlet 250°C, transfer line 280°C, ion source 230°C, and quadrupole 150°C. Mass spectra were collected from 80 to 600 m/z under selective ion monitoring mode. The data was analyzed by Agilent MassHunter Quantitative Analysis Software and natural abundance was corrected by ISOCOR software. Metabolite concentrations were determined from standard curves.

Bioinformatics—Collection and analysis of scRNASeq reads has been described in detail.[15] Briefly, reads were demultiplexed and aligned to a human transcriptomic reference (GRCh38) with Cell Ranger software. The resulting digital gene expression matrices representing the transcript counts for each gene in each cell were combined for all samples and analyzed using R statistical language methods.[71] A threshold of 600 detected genes per cell was applied to filter out low quality cells or debris, and the median number of genes and transcripts detected per cell was 1314 and 2577, respectively. t-distributed stochastic neighbor embedding (t-SNE) was used to visualize cell clusters.

QUANTIFICATION AND STATISTICAL ANALYSIS

Blinding—Researchers evaluating ERG, immunostaining, and mass spec were blinded as to genotype.

Sample size—Based on standard deviations derived from our previous extensive studies of ERG, photoreceptor numbers in WT and RP animals,[5,9] we calculated three samples would be sufficient to detect a 30% change with a confidence of 0.95 in each of these measurements. Note that all changes (e.g., WT vs. RP) exceed 30% and n was 3 or greater. For mass spec analysis, the number of animals and independent samples is presented in figure legends and exceeds the number we found previously would be sufficient to observe a 30% change with a confidence of 0.95.[9]

Data inclusion/exclusion—See data analysis for outlier exclusion criteria in metabolite import from and export into the choroid circulation.

Replicates—Each experiment was repeated at least three time. The number of animals evaluated is shown in the figure legends. For ERGs, 30 replicates were averaged for each eye.

Significance—Significance was calculated by Student’s t-test. Error bars in figures show standard deviations or errors of the mean as indicated.

Metabolite data analysis—All raw data were organized by metabolites into rows and animal collection sites into columns. Correction was performed to the control (Myristic Acid-D27 for GC/MS and Nicotinamide D4 for LC/MS). Artery averages in a pig were subtracted from the four vortex veins. $n = 6$, with three independent blood collections. Results are presented using the four vortex veins independently and as an average of the four veins. Data points were entered into GraphPad Prism 9 as columns of data for each metabolite. Outliers were detected and removed using Prism’s ROUT method. This method identifies outliers using nonlinear regression based on the false discovery rate and a robust mean. This method detects any number of outliers (up to 30% of the sample size). The false discovery rate and its statistical value, Q, is the chance of falsely identifying one or more outliers. Q was set to the value of $Q = 0.2\%$. At $Q = 0.2\%$, no more than 2% of the identified outliers were false and at least 98% to be actual, true outliers. After outliers were detected and removed, ordinary one-way ANOVA analysis was used to determine the statistical difference of means between the four vortex veins (IN, IT, SN, ST) with the assumptions that the data represents a Gaussian distribution and consists of equal standard deviations with no matching, pairing, or repeated measures of datasets. To find the statistical differences of the veins, the mean of each column was compared to all other columns, showing statistical differences. Correction for the family errors brought about by the multiple comparisons was performed using the Tukey *post hoc* test based on a family-wise alpha of 0.05 (95% confidence interval). p values are shown on graphs for comparisons meeting the threshold of $p < 0.05$. The analyzed p value is shown on the line corresponding to the statistical difference presented. No residuals were analyzed for diagnostics (heteroscedasticity or Gaussian distribution).

For the AM-to-PM groups, all group-corrected and artery-subtracted data points for the morning animals and all data points for the afternoon animals were entered as separate columns for analysis. Outlier detection was performed as above. With outliers removed, Prism’s built-in unpaired student t-test was performed assuming a Gaussian distribution and equal standard deviations. Calculations are based on two-tailed analysis using a confidence level of 95% and definition of statistical difference as $p < 0.05$. Statistical differences between the AM and PM groups are shown with lines denoting differences of $p < 0.05$ only. No diagnostics of residuals were performed.

Supplementary Material

Refer to Web version on PubMed Central for supplementary material.

ACKNOWLEDGMENTS

We thank Josh Sanes for helpful comments on the manuscript and Patrick Scott for EM images. These studies were supported by grants from the NEI, BrightFocus Foundation, and Research to Prevent Blindness.

REFERENCES

1. Hanany M, Rivolta C, and Sharon D (2020). Worldwide carrier frequency and genetic prevalence of autosomal recessive inherited retinal diseases. Proc. Natl. Acad. Sci. USA 117, 2710–2716. 10.1073/pnas.1913179117. [PubMed: 31964843]
2. Aït-Ali N, Fridlich R, Millet-Puel G, Clérin E, Delalande F, Jaillard C, Blond F, Perrocheau L, Reichman S, Byrne LC, et al. (2015). Rod-derived cone viability factor promotes cone survival by stimulating aerobic glycolysis. Cell 161, 817–832. 10.1016/j.cell.2015.03.023. [PubMed: 25957687]
3. Petit L, Ma S, Cipi J, Cheng SY, Zieger M, Hay N, and Punzo C (2018). Aerobic Glycolysis Is Essential for Normal Rod Function and Controls Secondary Cone Death in Retinitis Pigmentosa. Cell Rep. 23, 2629–2642. 10.1016/j.celrep.2018.04.111. [PubMed: 29847794]
4. Chinchore Y, Begaj T, Wu D, Drokhlyansky E, and Cepko CL (2017). Glycolytic reliance promotes anabolism in photoreceptors. Elife 6, e25946. 10.7554/eLife.25946. [PubMed: 28598329]
5. Wang W, Lee SJ, Scott PA, Lu X, Emery D, Liu Y, Ezashi T, Roberts MR, Ross JW, Kaplan HJ, and Dean DC (2016).Two-Step Reactivation of Dormant Cones in Retinitis Pigmentosa. Cell Rep. 15, 372–385. 10.1016/j.celrep.2016.03.022. [PubMed: 27050517]
6. Daniele LL, Han JYS, Samuels IS, Komirisetty R, Mehta N, McCord JL, Yu M, Wang Y, Boesze-Battaglia K, Bell BA, et al. (2022). Glucose uptake by GLUT1 in photoreceptors is essential for outer segment renewal and rod photoreceptor survival. Faseb. J 36, e22428. 10.1096/fj.202200369R. [PubMed: 35766190]
7. Swarup A, Samuels IS, Bell BA, Han JYS, Du J, Massenzio E, Abel ED, Boesze-Battaglia K, Peachey NS, and Philp NJ (2019). Modulating GLUT1 expression in retinal pigment epithelium decreases glucose levels in the retina: impact on photoreceptors and Mµller glial cells. Am. J. Physiol. Cell Physiol 316, C121–C133. 10.1152/ajpcell.00410.2018. [PubMed: 30462537]
8. Ruggiero L, Connor MP, Chen J, Langen R, and Finnemann SC (2012). Diurnal, localized exposure of phosphatidylserine by rod outer segment tips in wild-type but not Itgb5−/− or Mfge8−/− mouse retina. Proc. Natl. Acad. Sci. USA 109, 8145–8148. 10.1073/pnas.1121101109. [PubMed: 22566632]
9. Wang W, Kini A, Wang Y, Liu T, Chen Y, Vukmanic E, Emery D, Liu Y, Lu X, Jin L, et al. (2019). Metabolic Deregulation of the Blood-Outer Retinal Barrier in Retinitis Pigmentosa. Cell Rep. 28, 1323–1334.e4. 10.1016/j.celrep.2019.06.093. [PubMed: 31365873]
10. Ross JW, Fernandez de Castro JP, Zhao J, Samuel M, Walters E, Rios C, Bray-Ward P, Jones BW, Marc RE, Wang W, et al. (2012). Generation of an inbred miniature pig model of retinitis pigmentosa. Invest. Ophthalmol. Vis. Sci 53, 501–507. 10.1167/iovs.11-8784. [PubMed: 22247487]
11. Wang W, Fernandez de Castro J, Vukmanic E, Zhou L, Emery D, Demarco PJ, Kaplan HJ, and Dean DC (2011). Selective rod degeneration and partial cone inactivation characterize an iodoacetic acid model of Swine retinal degeneration. Invest. Ophthalmol. Vis. Sci 52, 7917–7923. 10.1167/iovs.11-7849. [PubMed: 21896868]
12. Wang W, Zhou L, Lee SJ, Liu Y, Fernandez de Castro J, Emery D, Vukmanic E, Kaplan HJ, and Dean DC (2014). Swine cone and rod precursors arise sequentially and display sequential and transient integration and differentiation potential following transplantation. Invest. Ophthalmol. Vis. Sci 55, 301–309. 10.1167/iovs.13-12600. [PubMed: 24327609]
13. Perlman I, Kondo M, Chelva E, Robson AG, and Holder GE (2020). ISCEV extended protocol for the S-cone ERG. Doc. Ophthalmol 140, 95–101. 10.1007/s10633-019-09730-6. [PubMed: 31749034]
14. Sustar M, Hawlina M, and Brecelj J (2011). Electroretinographic evaluation of the retinal S-cone system. Doc. Ophthalmol 123, 199–210. 10.1007/s10633-011-9299-5. [PubMed: 22120511]
15. Yan W, Peng YR, van Zyl T, Regev A, Shekhar K, Juric D, and Sanes JR (2020). Cell Atlas of The Human Fovea and Peripheral Retina. Sci. Rep 10, 9802. 10.1038/s41598-020-66092-9. [PubMed: 32555229]

16. Nadal-Nicolás FM, Kunze VP, Ball JM, Peng BT, Krishnan A, Zhou G, Dong L, and Li W (2020). True S-cones are concentrated in the ventral mouse retina and wired for color detection in the upper visual field. Elife 9, e56840. 10.7554/eLife.56840. [PubMed: 32463363]
17. Rajala A, Gupta VK, Anderson RE, and Rajala RVS (2013). Light activation of the insulin receptor regulates mitochondrial hexokinase. A possible mechanism of retinal neuroprotection. Mitochondrion 13, 566–576. 10.1016/j.mito.2013.08.005. [PubMed: 23993956]
18. Grenell A, Wang Y, Yam M, Swarup A, Dilan TL, Hauer A, Linton JD, Philp NJ, Gregor E, et al. (2019). Loss of MPC1 reprograms retinal metabolism to impair visual function. Proc. Natl. Acad. Sci. USA 116, 3530–3535. 10.1073/pnas.1812941116. [PubMed: 30808746]
19. Swaroop A, Kim D, and Forrest D (2010). Transcriptional regulation of photoreceptor development and homeostasis in the mammalian retina. Nat. Rev. Neurosci 11, 563–576. 10.1038/nrn2880. [PubMed: 20648062]
20. Ames A 3rd, Li YY, Heher EC, and Kimble CR (1992). Energy metabolism of rabbit retina as related to function: high cost of Na+ transport. J. Neurosci 12, 840–853. 10.1523/jneurosci.12-03-00840.1992. [PubMed: 1312136]
21. Ball JM, Chen S, and Li W (2022). Mitochondria in cone photoreceptors act as microlenses to enhance photon delivery and confer directional sensitivity to light. Sci. Adv 8, eabn2070. 10.1126/sciadv.abn2070. [PubMed: 35235359]
22. Wan QL, Meng X, Wang C, Dai W, Luo Z, Yin Z, Ju Z, Fu X, Yang J, Ye Q, et al. (2022). Histone H3K4me3 modification is a transgenerational epigenetic signal for lipid metabolism in Caenorhabditis elegans. Nat. Commun 13, 768. 10.1038/s41467-022-28469-4. [PubMed: 35140229]
23. Zhang B, Zhou BH, Xiao M, Li H, Guo L, Wang MX, Yu SH, and Ye QH (2020). KDM5C Represses FASN-Mediated Lipid Metabolism to Exert Tumor Suppressor Activity in Intrahepatic Cholangiocarcinoma. Front. Oncol 10, 1025. 10.3389/fonc.2020.01025. [PubMed: 32714863]
24. Rouillard AD, Gundersen GW, Fernandez NF, Wang Z, Monteiro CD, McDermott MG, and Ma'ayan A (2016). The harmonizome: a collection of processed datasets gathered to serve and mine knowledge about genes and proteins. Database 2016, baw100. 10.1093/database/baw100. [PubMed: 27374120]
25. Black JC, Van Rechem C, and Whetstine JR (2012). Histone lysine methylation dynamics: establishment, regulation, and biological impact. Mol. Cell 48, 491–507. 10.1016/j.molcel.2012.11.006. [PubMed: 23200123]
26. Abla H, Sollazzo M, Gasparre G, Iommarini L, and Porcelli AM (2020). The multifaceted contribution of α-ketoglutarate to tumor progression: An opportunity to exploit? Semin. Cell Dev. Biol 98, 26–33. 10.1016/j.semcdb.2019.05.031. [PubMed: 31175937]
27. Jang C, Hui S, Zeng X, Cowan AJ, Wang L, Chen L, Morscher RJ, Reyes J, Frezza C, Hwang HY, et al. (2022). Metabolite Exchange between Mammalian Organs Quantified in Pigs. Cell Metabol. 34, 1410. 10.1016/j.cmet.2022.08.006.
28. Verma A, Bacci T, Sarraf D, Freund KB, and Sadda SR (2021). Vortex Vein Imaging: What Can It Tell Us? Clin. Ophthalmol 15, 3321–3331. 10.2147/opth.S324245. [PubMed: 34408390]
29. Singh C, Hoppe G, Tran V, McCollum L, Bolok Y, Song W, Sharma A, Brunengraber H, and Sears JE (2019). Serine and 1-carbon metabolism are required for HIF-mediated protection against retinopathy of prematurity. JCI Insight 4, e129398. 10.1172/jci.insight.129398. [PubMed: 31341109]
30. Mustafi D, Kevany BM, Genoud C, Bai X, and Palczewski K (2013). Photoreceptor phagocytosis is mediated by phosphoinositide signaling. Faseb. J 27, 4585–4595. 10.1096/fj.13-237537. [PubMed: 23913857]
31. Swarup A, Samuels IS, Bell BA, Han JYS, Du J, Massenzio E, Abel ED, Boesze-Battaglia K, Peachey NS, and Philp NJ (2019). Modulating GLUT1 expression in the RPE decreases glucose levels in the retina: Impact on photoreceptors and Muller glial cells. Am. J. Physiol. Cell Physiol 316, C121–C133. 10.1152/ajpcell.00410.2018. [PubMed: 30462537]
32. Choi I, Son H, and Baek JH (2021). Tricarboxylic Acid (TCA) Cycle Intermediates: Regulators of Immune Responses. Life 11, 69. 10.3390/life11010069. [PubMed: 33477822]

33. Hass DT, Bisbach CM, Robbings BM, Sadilek M, Sweet IR, and Hurley JB (2022). Succinate metabolism in the retinal pigment epithelium uncouples respiration from ATP synthesis. Cell Rep. 39, 110917. 10.1016/j.celrep.2022.110917. [PubMed: 35675773]
34. Bisbach CM, Hass DT, Robbings BM, Rountree AM, Sadilek M, Sweet IR, and Hurley JB (2020). Succinate Can Shuttle Reducing Power from the Hypoxic Retina to the O(2)-Rich Pigment Epithelium. Cell Rep. 31, 107606. 10.1016/j.celrep.2020.107606. [PubMed: 32375026]
35. Brisson L, Bański P, Sboarina M, Dethier C, Danhier P, Fontenille MJ, Van Hée VF, Vazeille T, Tardy M, Falces J, et al. (2016). Lactate Dehydrogenase B Controls Lysosome Activity and Autophagy in Cancer. Cancer Cell 30, 418–431. 10.1016/j.ccell.2016.08.005. [PubMed: 27622334]
36. Moran AL, Fehilly JD, Floss Jones D, Collery R, and Kennedy BN (2022). Regulation of the rhythmic diversity of daily photoreceptor outer segment phagocytosis in vivo. Faseb. J 36, e22556. 10.1096/fj.202200990RR. [PubMed: 36165194]
37. Connaughton V (1995). Glutamate and Glutamate Receptors in the Vertebrate Retina. In Webvision: The Organization of the Retina and Visual System, Kolb H, Fernandez E, and Nelson R, eds. (University of Utah Health Sciences Center Copyright: © 2023 Webvision).
38. Hasegawa J, Obara T, Tanaka K, and Tachibana M (2006). High-density presynaptic transporters are required for glutamate removal from the first visual synapse. Neuron 50, 63–74. 10.1016/j.neuron.2006.02.022. [PubMed: 16600856]
39. Hertz L (2013). The Glutamate-Glutamine (GABA) Cycle: Importance of Late Postnatal Development and Potential Reciprocal Interactions between Biosynthesis and Degradation. Front. Endocrinol 4, 59. 10.3389/fendo.2013.00059.
40. McKenna MC, Waagepetersen HS, Schousboe A, and Sonnewald U (2006). Neuronal and astrocytic shuttle mechanisms for cytosolic-mitochondrial transfer of reducing equivalents: current evidence and pharmacological tools. Biochem. Pharmacol 71, 399–407. 10.1016/j.bcp.2005.10.011. [PubMed: 16368075]
41. Palaiologos G, Hertz L, and Schousboe A (1988). Evidence that aspartate aminotransferase activity and ketodicarboxylate carrier function are essential for biosynthesis of transmitter glutamate. J. Neurochem 51, 317–320. 10.1111/j.1471-4159.1988.tb04872.x. [PubMed: 2898006]
42. Rosca MG, Vazquez EJ, Chen Q, Kerner J, Kern TS, and Hoppel CL (2012). Oxidation of fatty acids is the source of increased mitochondrial reactive oxygen species production in kidney cortical tubules in early diabetes. Diabetes 61, 2074–2083. 10.2337/db11-1437. [PubMed: 22586586]
43. Kuehne A, Emmert H, Soehle J, Winnefeld M, Fischer F, Wenck H, Gallinat S, Terstegen L, Lucius R, Hildebrand J, and Zamboni N (2015). Acute Activation of Oxidative Pentose Phosphate Pathway as First-Line Response to Oxidative Stress in Human Skin Cells. Mol. Cell 59, 359–371. 10.1016/j.molcel.2015.06.017. [PubMed: 26190262]
44. Xiao C, Fan T, Tian H, Zheng Y, Zhou Z, Li S, Li C, and He J (2021). H3K36 trimethylation-mediated biological functions in cancer. Clin. Epigenetics 13, 199. 10.1186/s13148-021-01187-2. [PubMed: 34715919]
45. Sen P, Dang W, Donahue G, Dai J, Dorsey J, Cao X, Liu W, Cao K, Perry R, Lee JY, et al. (2015). H3K36 methylation promotes longevity by enhancing transcriptional fidelity. Genes Dev. 29, 1362–1376. 10.1101/gad.263707.115. [PubMed: 26159996]
46. Liu M, Rao H, Liu J, Li X, Feng W, Gui L, Tang H, Xu J, Gao WQ, and Li L (2021). The histone methyltransferase SETD2 modulates oxidative stress to attenuate experimental colitis. Redox Biol. 43, 102004. 10.1016/j.redox.2021.102004. [PubMed: 34020310]
47. Quijano C, Trujillo M, Castro L, and Trostchansky A (2016). Interplay between oxidant species and energy metabolism. Redox Biol. 8, 28–42. 10.1016/j.redox.2015.11.010. [PubMed: 26741399]
48. Yuan H, Li N, Fu D, Ren J, Hui J, Peng J, Liu Y, Qiu T, Jiang M, Pan Q, et al. (2017). Histone methyltransferase SETD2 modulates alternative splicing to inhibit intestinal tumorigenesis. J. Clin. Invest 127, 3375–3391. 10.1172/jci94292. [PubMed: 28825595]
49. Yang L, and Chen LL (2014). Microexons go big. Cell 159, 1488–1489. 10.1016/j.cell.2014.12.004. [PubMed: 25525868]

50. Marasco LE, and Kornblihtt AR (2023). The physiology of alternative splicing. Nat. Rev. Mol. Cell Biol 24, 242–254. 10.1038/s41580-022-00545-z. [PubMed: 36229538]
51. Torres-Méndez A, Pop S, Bonnal S, Almudi I, Avola A, Roberts RJV, Paolantoni C, Alcaina-Caro A, Martín-Anduaga A, Haussmann IU, et al. (2022). Parallel evolution of a splicing program controlling neuronal excitability in flies and mammals. Sci. Adv 8, eabk0445. 10.1126/sciadv.abk0445. [PubMed: 35089784]
52. Sundar J, Matalkah F, Jeong B, Stoilov P, and Ramamurthy V (2021). The Musashi proteins MSI1 and MSI2 are required for photoreceptor morphogenesis and vision in mice. J. Biol. Chem 296, 100048. 10.1074/jbc.RA120.015714. [PubMed: 33168629]
53. Murphy D, Cieply B, Carstens R, Ramamurthy V, and Stoilov P (2016). The Musashi 1 Controls the Splicing of Photoreceptor-Specific Exons in the Vertebrate Retina. PLoS Genet. 12, e1006256. 10.1371/journal.pgen.1006256. [PubMed: 27541351]
54. Ciampi L, Mantica F, López-Blanch L, Permanyer J, Rodriguez-Marín C, Zang J, Cianferoni D, Jiménez-Delgado S, Bonnal S, Miravet-Verde S, et al. (2022). Specialization of the photoreceptor transcriptome by Srrm3-dependent microexons is required for outer segment maintenance and vision. Proc. Natl. Acad. Sci. USA 119, e2117090119. 10.1073/pnas.2117090119. [PubMed: 35858306]
55. Ohta S, Nishida E, Yamanaka S, and Yamamoto T (2013). Global splicing pattern reversion during somatic cell reprogramming. Cell Rep. 5, 357–366. 10.1016/j.celrep.2013.09.016. [PubMed: 24139801]
56. Iijima T, Hidaka C, and Iijima Y (2016). Spatio-temporal regulations and functions of neuronal alternative RNA splicing in developing and adult brains. Neurosci. Res 109, 1–8. 10.1016/j.neures.2016.01.010. [PubMed: 26853282]
57. Völkner M, Wagner F, Steinheuer LM, Carido M, Kurth T, Yazbeck A, Schor J, Wieneke S, Ebner LJA, Del Toro Runzer C, et al. (2022). HBEGF-TNF induce a complex outer retinal pathology with photoreceptor cell extrusion in human organoids. Nat. Commun 13, 6183. 10.1038/s41467-022-33848-y. [PubMed: 36261438]
58. Xie J, Zhu R, Peng Y, Gao W, Du J, Zhao L, Chi Y, and Yang L (2017). Tumor necrosis factor-alpha regulates photoreceptor cell autophagy after retinal detachment. Sci. Rep 7, 17108. 10.1038/s41598-017-17400-3. [PubMed: 29215050]
59. Nelson CM, Ackerman KM, O'Hayer P, Bailey TJ, Gorsuch RA, and Hyde DR (2013). Tumor necrosis factor-alpha is produced by dying retinal neurons and is required for Muller glia proliferation during zebrafish retinal regeneration. J. Neurosci 33, 6524–6539. 10.1523/jneurosci.3838-12.2013. [PubMed: 23575850]
60. Ciesla J, Moreno I Jr., and Munger J (2022). TNFα-induced metabolic reprogramming drives an intrinsic anti-viral state. PLoS Pathog. 18, e1010722. 10.1371/journal.ppat.1010722. [PubMed: 35834576]
61. Zhang DW, Shao J, Lin J, Zhang N, Lu BJ, Lin SC, Dong MQ, and Han J (2009). RIP3, an energy metabolism regulator that switches TNF-induced cell death from apoptosis to necrosis. Science 325, 332–336. 10.1126/science.1172308. [PubMed: 19498109]
62. Yu Z, Chen F, Liu H, Fan J, Ding X, Zhu X, Cui S, Yi H, Zhou X, Hu Y, and Liu W (2022). Silencing CoREST inhibits the viability and migration of fibroblast-like synoviocytes in TNF-α-induced rheumatoid arthritis. Exp. Ther. Med 23, 148. 10.3892/etm.2021.11071. [PubMed: 35069829]
63. Liu R, Liu W, Doctrow SR, and Baudry M (2003). Iron toxicity in organotypic cultures of hippocampal slices: role of reactive oxygen species. J. Neurochem 85, 492–502. 10.1046/j.1471-4159.2003.01708.x. [PubMed: 12675926]
64. Han JYS, Kinoshita J, Bisetto S, Bell BA, Nowak RA, Peachey NS, and Philp NJ (2020). Role of monocarboxylate transporters in regulating metabolic homeostasis in the outer retina: Insight gained from cell-specific Bsg deletion. Faseb. J 34, 5401–5419. 10.1096/fj.201902961R. [PubMed: 32112484]
65. Kim JW, Yang HJ, Oel AP, Brooks MJ, Jia L, Plachetzki DC, Li W, Allison WT, and Swaroop A (2016). Recruitment of Rod Photoreceptors from Short-Wavelength-Sensitive Cones during the Evolution of Nocturnal Vision in Mammals. Dev. Cell 37, 520–532. 10.1016/j.devcel.2016.05.023. [PubMed: 27326930]

66. Popova EY, Pinzon-Guzman C, Salzberg AC, Zhang SSM, and Barnstable CJ (2016). LSD1-Mediated Demethylation of H3K4me2 Is Required for the Transition from Late Progenitor to Differentiated Mouse Rod Photoreceptor. Mol. Neurobiol 53, 4563–4581. 10.1007/s12035-015-9395-8. [PubMed: 26298666]

67. Sakami S, Maeda T, Bereta G, Okano K, Golczak M, Sumaroka A, Roman AJ, Cideciyan AV, Jacobson SG, and Palczewski K (2011). Probing mechanisms of photoreceptor degeneration in a new mouse model of the common form of autosomal dominant retinitis pigmentosa due to P23H opsin mutations. J. Biol. Chem 286, 10551–10567. 10.1074/jbc.M110.209759. [PubMed: 21224384]

68. Morén H, Gesslein B, Undrén P, Andreasson S, and Malmsjö M (2011). Endovascular coiling of the ophthalmic artery in pigs to induce retinal ischemia. Invest. Ophthalmol. Vis. Sci 52, 4880–4885. 10.1167/iovs.11-7628. [PubMed: 21622700]

69. Kanow MA, Giarmarco MM, Jankowski CS, Tsantilas K, Engel AL, Du J, Linton JD, Farnsworth CC, Sloat SR, Rountree A, et al. (2017). Biochemical adaptations of the retina and retinal pigment epithelium support a metabolic ecosystem in the vertebrate eye. Elife 6, e28899. 10.7554/eLife.28899. [PubMed: 28901286]

70. Zhang L, Du J, Justus S, Hsu CW, Bonet-Ponce L, Wu WH, Tsai YT, Wu WP, Jia Y, Duong JK, et al. (2016). Reprogramming metabolism by targeting sirtuin 6 attenuates retinal degeneration. J. Clin. Invest 126, 4659–4673. 10.1172/JCI86905. [PubMed: 27841758]

71. Peng YR, Shekhar K, Yan W, Herrmann D, Sappington A, Bryman GS, van Zyl T, Do MTH, Regev A, and Sanes JR (2019). Molecular Classification and Comparative Taxonomics of Foveal and Peripheral Cells in Primate Retina. Cell 176, 1222–1237.e22. 10.016/j.cell.2019.01.004. [PubMed: 30712875]

Highlights

- A Metabolic switch protects cone photoreceptors in retinitis pigmentosa progression
- Distinct metabolomes highlight the different photoreceptor types
- S cones show early vulnerability in retinitis pigmentosa

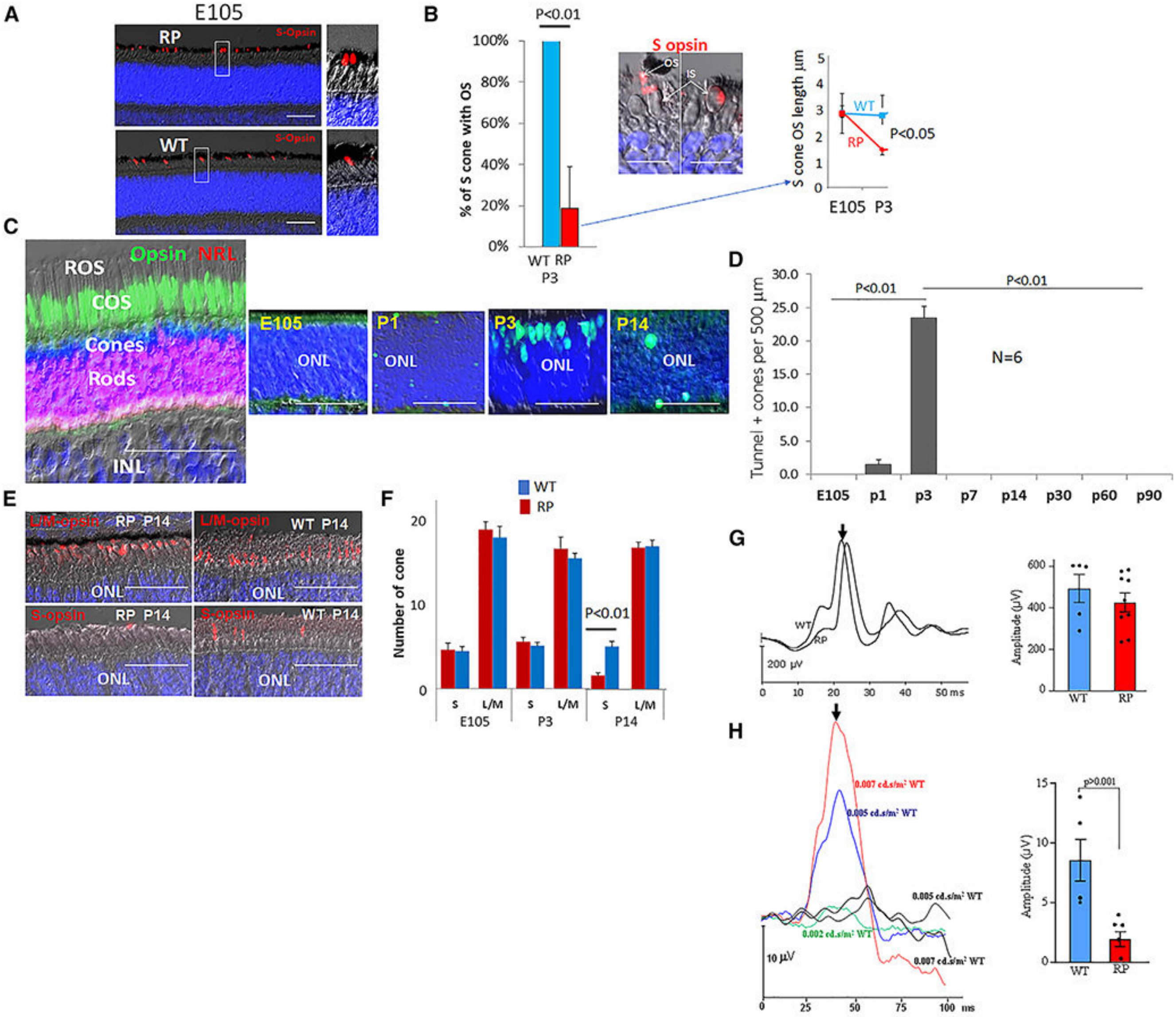

Figure 1. S cones show rapid loss of OS and apoptosis in RP, consistent with diminished activity

(A) WT and RP pig retinal sections on embryonic day 105 (E105; gestation is 113 days) were immunostained for S opsin. Boxed areas are shown at higher power on the right.

(B) The fraction of S opsin+ cones containing an OS in 200-μm lengths through the visual streak at P3. n = 6.S opsin immunostaining illustrates S cones with OS and those with only an inner segment (IS). Shown is the average length of OS in WT and RP (only S cones containing an OS) on P3.

(C) On the left, immunostaining for L/M opsin (Opsin) identifies cone OS (COS), and NRL marks rods. TUNEL staining identifies apoptotic cells at the indicated ages.

(D) Results from (C) were quantified by counting TUNEL+ cones in 500-μm lengths through the visual streak of RP pigs at the indicated ages. n = 6.

(E) Immunostaining for S and L/M opsins on P14 in WT and RP retinas as in (C).

(F) The number of S and L/M cones in WT and RP pigs at the indicated ages was quantified in 200-μm lengths through the visual streak. S opsin+ cell bodies were counted without regard to OS status. n = 6. Scale bars: 50 μm; 25 μm in (B).

(G) WT and RP pigs between P75 and P100 were light adapted to the standard ISCEV background of 30 cd/m^2 for 10 min, and photopic cone-mediated ERG waveforms (primarily from L/M cones) were recorded in response to ISCEV standard flashes of 3 cd s/m^2. Representative ERGs are shown along with quantification of b-wave amplitudes at ~20 ms (arrow).

(H) L/M cones were saturated before presentation of blue flash stimuli (LED: 455 nm) ranging from 0.002–0.06 cd s/m^2 in an S cone ISCEV protocol[13] (STAR Methods). Cone-mediated ERG responses were collected in WT and RP pigs as in (H), beginning with the lowest flash intensity. The S cone response is centered around 45 ms[13] (arrow). Representative ERG tracings are shown with blue flash stimuli at 0.002, 0.005, and 0.007 cd s/m^2, along with quantification of amplitudes at 0.005 cd s/m^2.

Error bars indicate standard error of the mean (STAR Methods). Significance was calculated by Student’s t test.

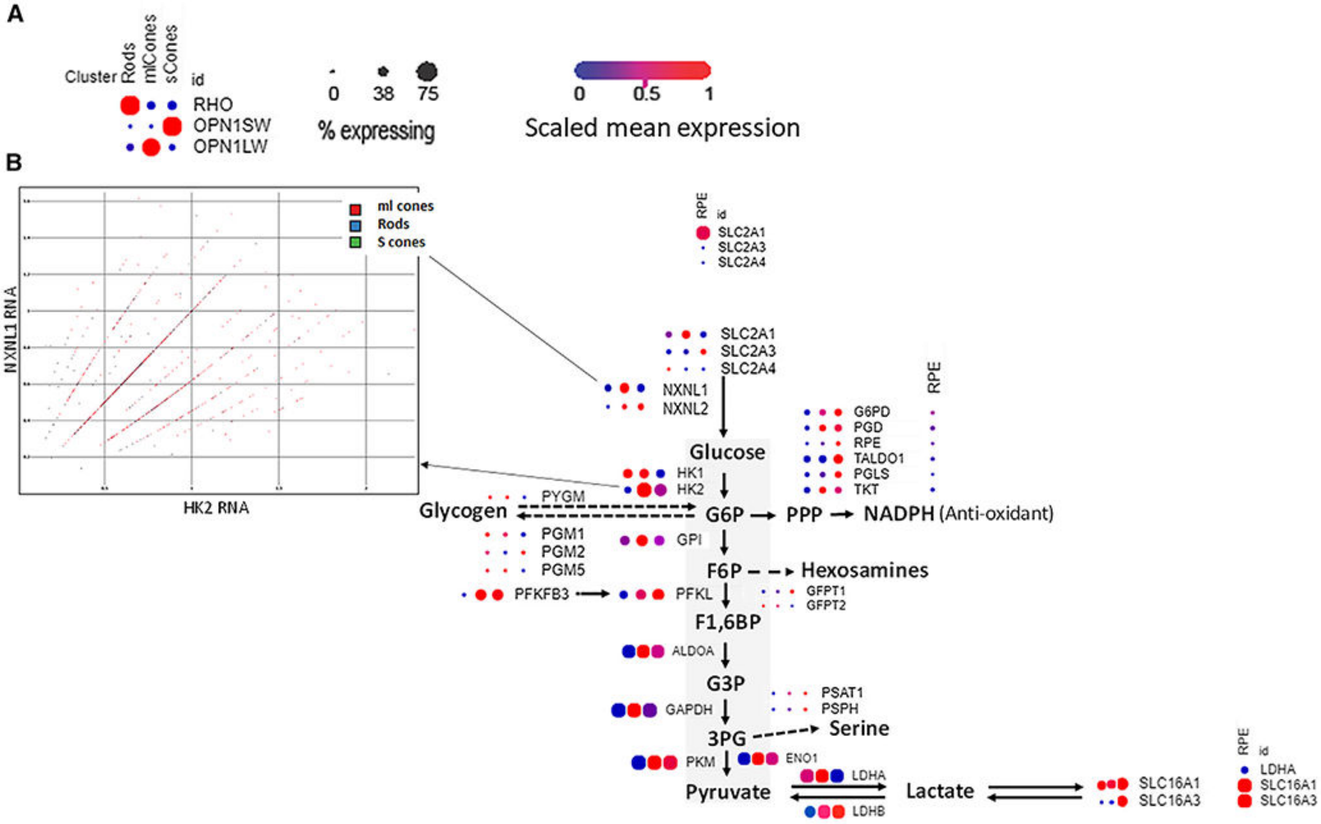

Figure 2. Photoreceptor metabolic transcriptomes suggest that rods are restricted to aerobic glycolysis, L/M cones have potential for aerobic glycolysis and oxidative phosphorylation, and S cones rely on oxidative phosphorylation

(A) 86,253 single-cell transcriptomes from retinas of seven human donors were separated into clusters in tSNE plots (Figure S2). Expression of the visual pigment genes *RHO, OPN1SW*, and *OPN1LW* highlighted independently clustering rods (6,073 cells), S cones (58 cells), and L/M cones (1,938 cells). Dot plots quantify expression level by color and percentage of cells expressing opsin RNAs by diameter in photoreceptor cell clusters.

(B)Expression of genes linked to glucose uptake and transition through glycolysis in photoreceptors. The rod, L/M cone, S cone dot plot order in (A) is maintained. A scatterplot compares expression of NXNl1 and HK2 RNAs in photoreceptors. The blue arc illustrates the cell surface.

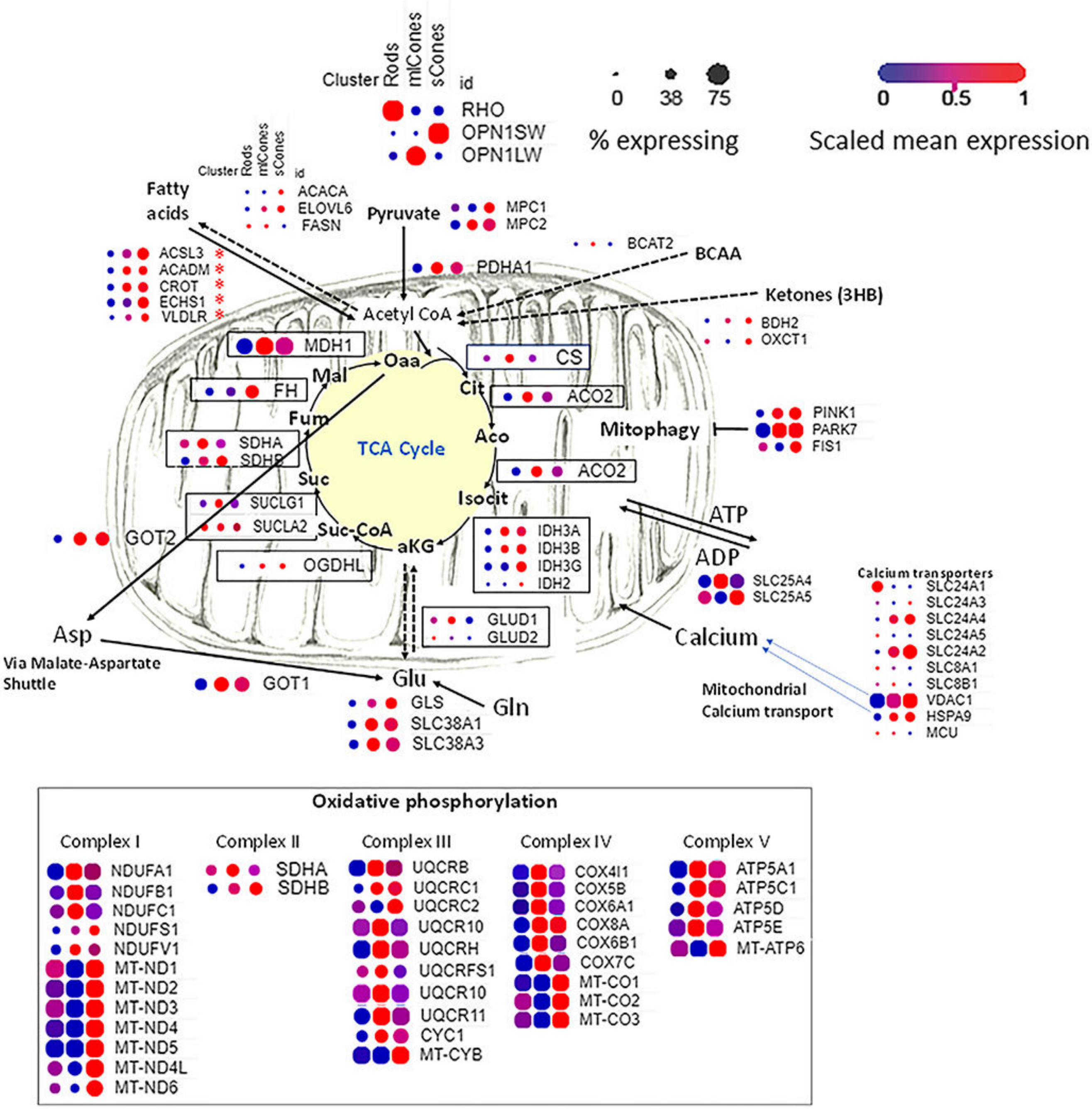

Figure 3. Photoreceptor mitochondrial transcriptomes

(A and B) Dot plots quantify the level of RNA expression and percentage of cells expressing in clusters of rods (left), L/M cones (center), and S cones (right) as in Figure 2. OAA, oxaloacetate; Cit, citrate; Aco, aconitate; isocit, isocitrate; aKG, α-ketoglutarate; Suc-CoA, succinyl CoA; Suc, succinate; Fum, fumarate; Mal, malate.

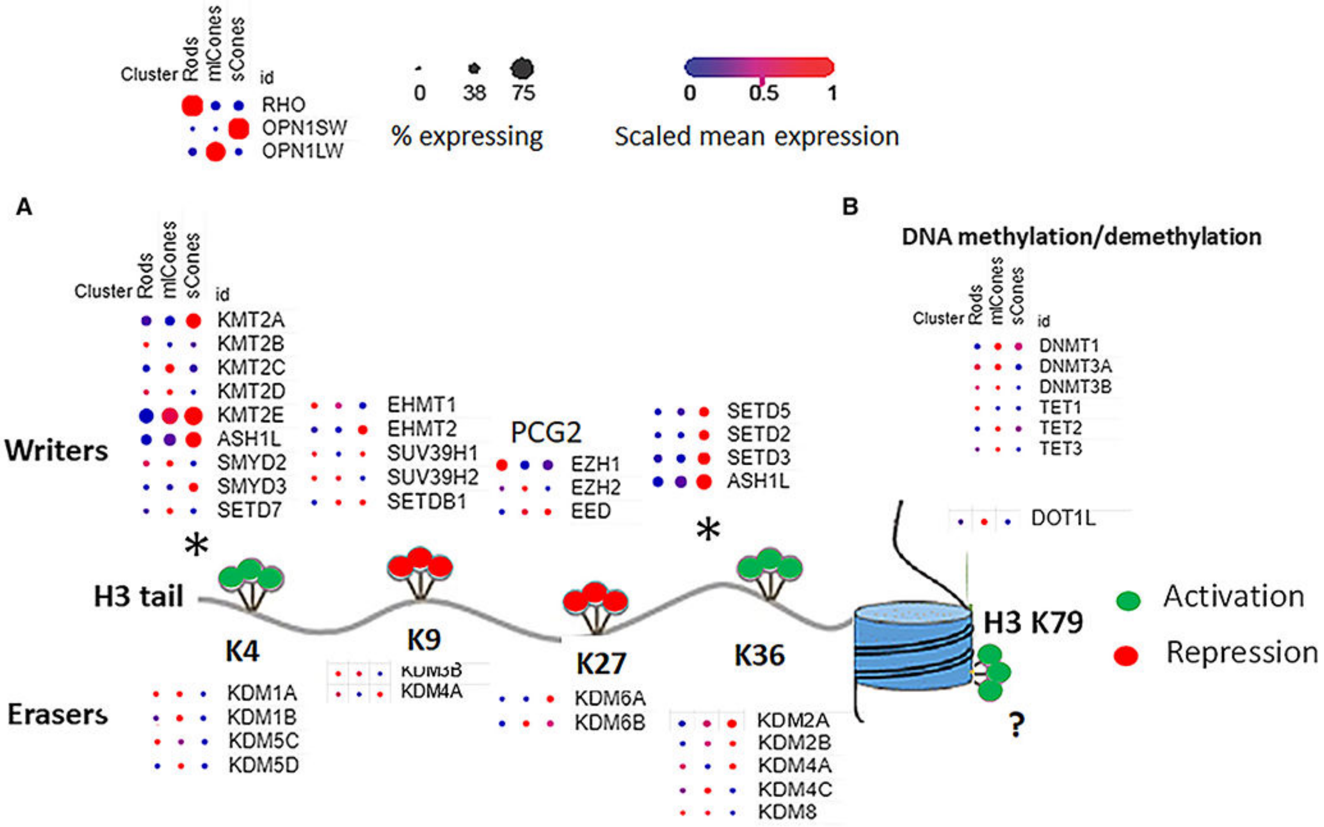

Figure 4. Photoreceptor histone modification transcriptomes

(A) Dot plots quantify RNA expression and percentage of cells expressing histone methylation writers and erasers, as in Figures 2 and 3. Black asterisks show a balance of writer vs. eraser RNAs favoring H3K4 and H3K36 methylation in S cones.

(B) RNAs regulating DNA methylation/demethylation are low/not detected in photoreceptors.

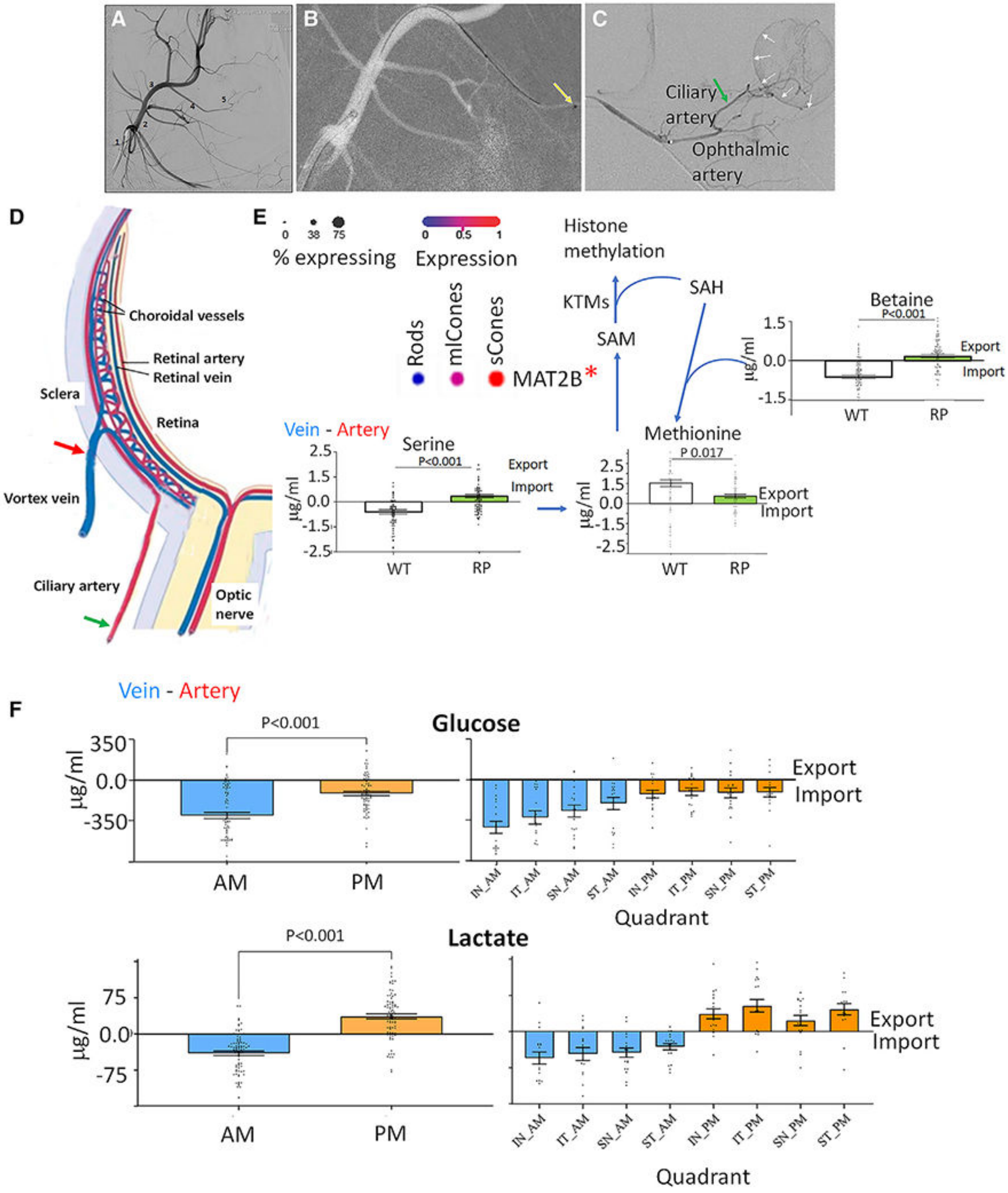

Figure 5. Choroidal transport of metabolites linked to histone methylation and metabolism

(A)Angiogram of the pig ciliary artery (STAR Methods) used to investigate metabolite import from and export into the choroid circulation and deliver ^{13}C metabolic fuels to the outer retina. Shown is a lateral view of the external maxillary artery (2), which branches from the external carotid artery (1) and gives rise to the intraorbital artery (3). The ophthalmic artery (4) branches off the infraorbital and gives rise to the ciliary artery (5) and central retinal artery (6).

(B) Position of the microcatheter (yellow arrow) and the microwire being used to extend the microcatheter, shown with contrast medium.

(C) Magnified image of the intra-arterial microcatheter in the ophthalmic artery, which forms the main ciliary artery. Contrast medium produces the characteristic crescent-shaped choroidal/retinal flush (white arrows). The microcatheter was moved to the ciliary artery (green arrow) from the ophthalmic artery to deliver metabolites or collect blood.

(D) Illustration of the choroid circulation, showing arterial blood entering the circulation via the ciliary artery and exiting the choroid via vortex veins that drain quadrants of the choroid. Import of metabolites from the circulation and export into the circulation were determined by comparing levels in arterial blood entering the choroid and veins draining the choroid using liquid chromatography-tandem mass spectrometry (LC-MS/MS) and gas chromatography (GC)-MS analysis (STAR Methods). The red arrow indicates a vortex vein exiting the choroid, and the green arrow indicates the ciliary artery entering the choroid. n = 6. Three independent blood samples were collected and analyzed, and an average of the four vortex veins was used. See Figure S5 for the four veins independently.

(E) Metabolite import from and export to the choroid circulation was determined by comparing levels in the artery and veins. n = 6. Three independent samples were collected and analyzed. The red asterisk indicates that *MAT2B* is a target of H3K36me3 (see text). See Figure S6 for analysis of the four vortex veins independently. RP indicates early RP after rod loss and S cone loss but before loss of L/M COS and photopic ERG (Figures 1G and 6A–6F).

(F) Glucose and lactate levels in the arterial and venous components of the choroid circulation were determined by mass spec as in (E). Blood was collected at 8:00 a.m. or 3:00 p.m. from pigs on a 12-h on/12-h off light cycle initiating at 6:00 a.m. n = 6. Three independent samples were collected and analyzed. On the left, an average of the four vortex veins is shown, and the veins are shown individually on the right.

Error bars are standard errors of the mean (STAR Methods). IN, inferior nasal vortex vein; IT, inferior temporal; SN, superior nasal; ST superior temporal. Significance was calculated by Student’s t test.

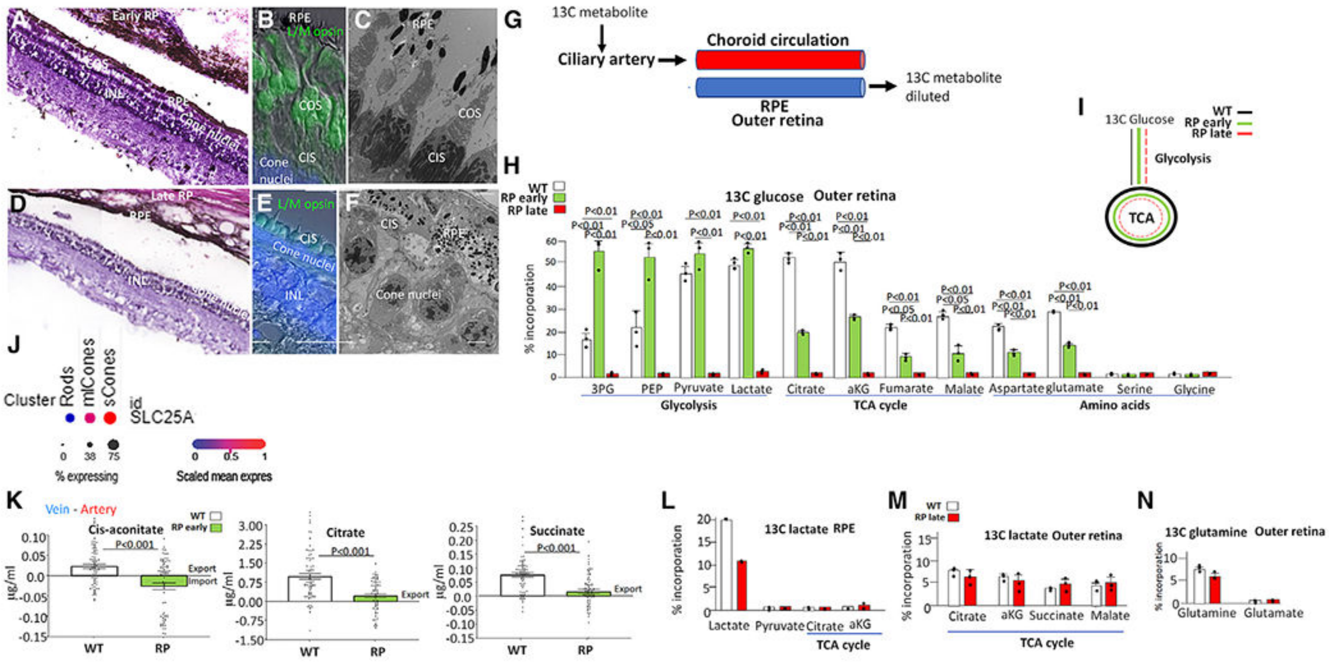

Figure 6. L/M cones shift toward aerobic glycolysis in early RP, and then glycolysis subsides in late RP

Lactate is imported from the choroid circulation during the period of new COS synthesis, and ^{13}C from lactate is incorporated into TCA cycle intermediates in the outer retina at similar levels in the WT and RP, but ^{13}C from lactate was not detected in TCA cycle metabolites in the RPE. A diminished TCA cycle impedes cone glutamate synthesis in RP.

(A) H&E section showing that the ONL has diminished to 1–2 rows of cones by 3 months of age in RP pigs (early RP).

(B) Immunostaining for L/M opsin shows persisting cone OS at this age.

(C) Electron microscopy (EM) showing representative cone ISs (CISs) and COSs.

(D) H&E section showing 1–2 rows of cones in RP at 12 months of age, where cones are functionally dormant (late RP).9

(E) Immunostaining for cone opsin shows that cones in late RP have lost OS.

(F) EM showing cones lacking outer segments.

Scale bars: 50 µm (A, B, D, and E) and 5 mm (C and F).

(G) Illustration showing ^{13}C metabolite injection into the ciliary artery, uptake by the RPE and outer retina, and dilution of ^{13}C metabolites as they exit the choroid into the general circulation.

(H) ^{13}C glucose was injected into the ciliary artery of WT and early and late RP pigs, and incorporation into the outer retina was analyzed by mass spec 30 min later (G; Figure 5; STAR Methods). n = 3. Error bars indicate standard deviation (STAR Methods).

(I) Summary of changes in glycolysis and the TCA cycle as RP progresses (see H).

(J) Dot plots showing induction of SLC25A in cones.

(K) Metabolite levels were measured by mass spec in the arterial circulation entering the choroid and in the four vortex veins draining quadrants of the choroid as in Figure 5 to follow export of TCA intermediates from the outer retina into the choroid circulation. An average of the four veins is shown. Results with individual veins are shown in Figure S6.

(L) ^{13}C lactate incorporation into TCA cycle intermediates in the outer retina is compared in the WT and RP.

(M) ^{13}C lactate is not metabolized into TCA cycle intermediates in the RPE in the WT or late RP. n = 3. Error bars indicate standard deviation.

(N) ^{13}C glutamine is not detected in glutamate in the WT or early RP outer retina. Significance was calculated by Student's t test.

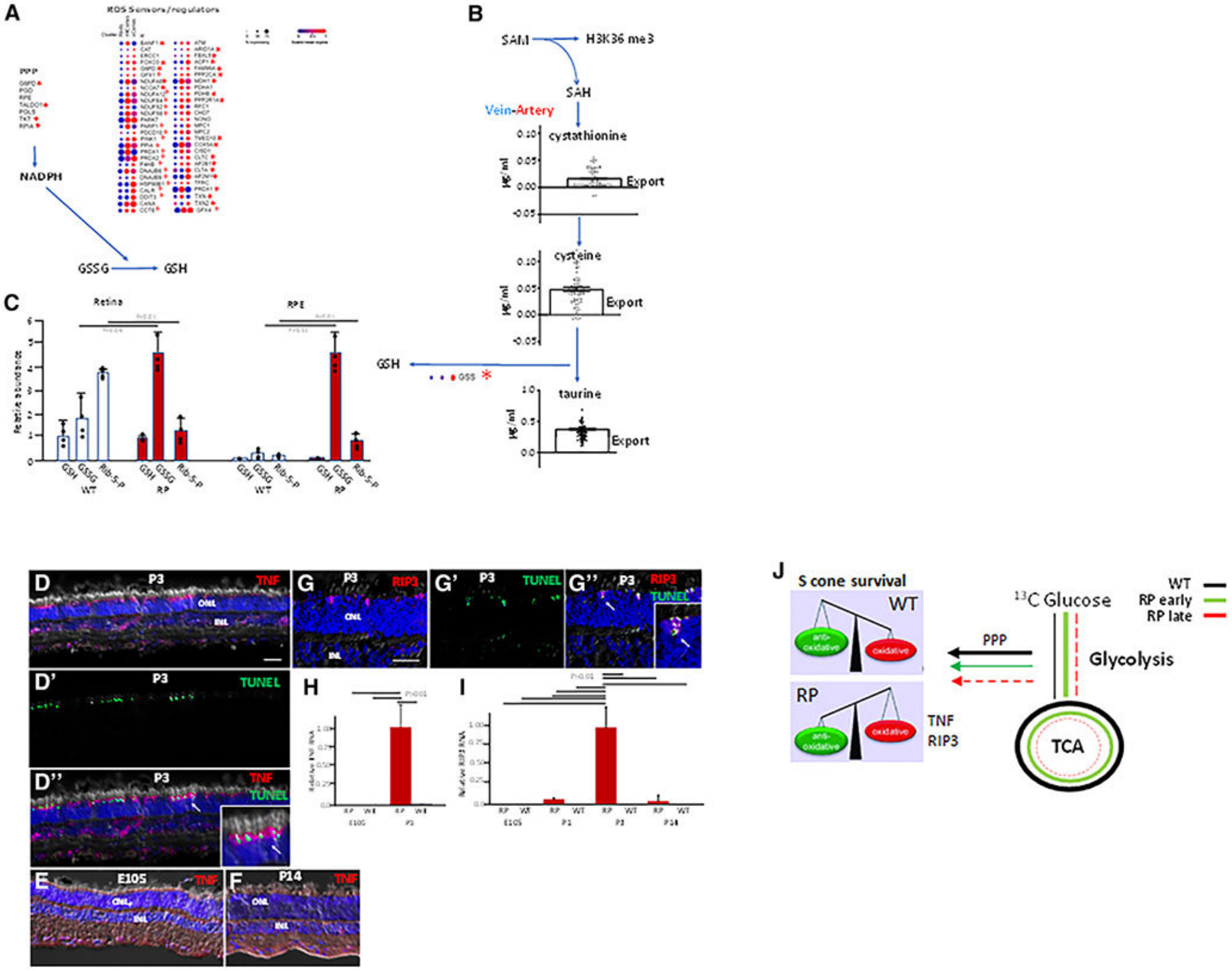

Figure 7. The S cone transcriptome shows induction of PPP and ROS response genes linked to H3K36 histone methylation, GSH oxidation increases in RP, and TNF and RIP3 are induced in apoptotic S cones in RP

(A) As in Figure 5, metabolite levels in arterial circulation entering the choroid were compared with levels in an average of the four vortex veins draining the choroid to determine import from and export to the choroid circulation. See Figure S6 for analysis of vortex veins individually. n = 6. Three independent samples were analyzed.

(B) Dot plots quantifying RNA expression and percentage of photoreceptor cell types expressing as in Figures 2 and 3. Red asterisks indicate genes targeted by H3K36me3 (see text).

(C) Steady-state levels of GSH, GSSG, and ribulose-5-phosphate (Rib-5-P; RIPA) determined by mass spec in the retina and RPE in the WT and RP. n = 4. Error bars indicate standard deviation (STAR Methods).

(D–D″) Immunostaining showing overlap in TUNEL and TNF immunostaining in RP on P3. A higher-power view of the region denoted by an arrow is shown as an inset in (D″). Scale bars: 50 μm.

(E and F) Immunostaining showing that TNF is not expressed in the RP retina on E105 before birth or on P14 after the burst of apoptosis.

(G–G″) Immunostaining showing that, like TNF, activated RIP3 (S227 phosphorylation) is expressed in TUNEL+ cones in RP on P3.

(H and I) Real-time PCR showing that TNF and RIP3 RNAs are induced in RP retinas at P3. n = 3. Error bars indicate standard deviation (STAR Methods).

(J) Illustration showing loss of the PPP in S cones and induction of TNF-RIP3 causing early S cone death in RP. Significance was calculated by Student’s t test.

KEY RESOURCES TABLE

REAGENT or RESOURCE	SOURCE	IDENTIFIER
Antibodies		
TNFa	abcam	183218; RRID:AB_2889388
RIP3S227	abcam	209384; RRID:AB_2714035
L/M opsins	millipore	5405; RRID:AB_177456
S opsin	Millipore	Ab5407; RRID:AB_177457
nrl	Anand Swaroop	N/A
L opsin/JH492	Jeremy Nathans	N/A
M opsin/JH455	Jeremy Nathans	N/A
Critical commercial assays		
TUNEL kit	Promega	G3250
MxP Quant 500 96 well plates	Biocrates	MxP® Quant 500
Experimental models: Organisms/strains		
RP pigs	National swine resource center	https://nsrrc.missouri.edu/
RP mice	Jackson laboratory	https://www.jax.org/strain/017628
Software and algorithms		
MetIDQ sortware	Biocrates	MetIDQ sortware
MultiQuant	AB Sciex	3.0.2 software
MassHunter Quantitative Analysis Software	Agilent	MassHunter Software
ISOCOR software	Agilent	ISOCOR software
Cell ranger software	10X Genomics	Cell ranger software
GraphPad Prism 9	GraphPad	GraphPad Prism 9